POLITECNICO DI MILANO

MASTER's Degree in ENGINEERING PHYSICS

MASTER's Degree Thesis

SUBNANOSECOND MAGNETO-OPTIC PROBING OF A SUPERCONDUCTOR USING A CONTINUOUS-WAVE LASER

Supervisors

Prof. GIACOMO GHIRINGHELLI

Prof. ANDREA CAVALLERI

Dr. GREGOR JOTZU

Candidate

JACOPO L.L. ALBERGONI

JULY 2021

Abstract

The expulsion of an external magnetic field upon cooling, known as the Meissner-Ochsenfeld effect, is an essential feature of superconductivity. Recently, experiments on a number of materials have shown evidence of light-induced superconductivity, based on the optical conductivity extracted from THz reflectivity measurements. Sensing an expulsion of a magnetic field in such a state would be a milestone on the path towards the understanding and control of complex quantum systems. In 2021 evidence of a light-induced superconductor with a lifetime larger than 10 ns has been reported. To characterize this state, a continuous-wave magneto-optic detection setup has been developed based on a helium-neon continuous-wave probe laser. The technique achieves a sensitivity of 0.6 $\mu\mathrm{T}/\sqrt{\mathrm{Hz}}$, along with a sub-nanosecond time resolution which allows a fast and accurate measurement of a magnetic field change upon mid-infrared excitation. The method has been tested on a set of different laser-driven materials: indium antimonide, bismuth-substituted yttrium-iron garnet and on an alkali-doped fulleride K_3C_{60} pellet. In the latter, the dynamics of the destruction of superconductivity has been characterized. The technique also opens up the possibility to study a wide range of other metastable light-induced states of matter, especially magnetic systems.

Acknowledgements

Working at Max Planck Institute for the Structure and Dynamics of Matter was the best way to finish my academic journey. I learnt so much and I want to thank Professor Giacomo Ghiringhelli and Professor Andrea Cavalleri for the opportunity and the trust. Gregor Jotzu thank you for all the time you spent training me, from the discussions to the optical table tips, without you this thesis project would not be a thing. A mention is due to my dare office mate Giovanni De Vecchi; to Sebastian Fava for being the best Hamburg guide, and to Michele Buzzi and Daniele Nicoletti for the italian fellowship. Thanks also to Ankit Disa, Thomas Gebert, Matthias Budden, Albert Liu and Edward Rowe for all the help, the questions you answered and the nice coffee breaks. Thanks to all the Cavalleri's group that I didn't mention, I already miss you. I must thanks my Hamburg friends with who I spent so many good moments during the last locked-down year, I don't know where I'd be without our brunches, trips and not-so-legal gathering. Last but not least thanks to my family who supported me during these six years of studying, fun, complaining and joy. This is for you.

Table of Contents

Introduction & Motivation

In classical solid state physics, electronic correlations can be treated in the perturbation theory framework, since their characteristic energy is much lower than the kinetic energy and the electron-phonon coupling of the system. In some peculiar complex solids, electronic correlations energy is dominant, giving rise to a wide variety of new solid state phases, often preserving quantum properties up to high temperature and in a macroscopic scale. Superconductivity, Mott physics and ferromagnetism are few example of the apparently infinite range of phenomena reachable by the exploitation of this high non-linear physics of strongly interacting many body systems. There are different factors involved in the competition between ground states of a system e.g. doping, pressure and external magnetic field [1]. If one excites the system with light, a redistribution of the electronic charges or a lattice rearrangement can be induced adding a degree of freedom at this artificial control of the material phase. Light can be used to manipulate excitations coherently, driving phonons and Josephson excitations, as well as charge and orbitals state. One of the main recent discovery in this field is the evidence of light-induced superconductivity in cuprates [2] and in the organic superconductor K_3C_{60} [3]. The astonishing finding of a metastable light-induced superconductive state in K_3C_{60} is the starting point of this thesis work.

In 2021 Budden et al. discovered a metastable light-induced superconductive state above critical temperature in K_3C_{60} lasting more than 10 nanoseconds [4]. This opened the possibility of a direct electronic measurement of the resistance, which dropped to zero as expected and which confirmed the optical conductivity results shown by Mitrano et al. in 2016 [3]. A very important step in the light control of this macroscopic quantum phase would be probing the light induced Meissner effect, i.e. the complete or partial expulsion of the magnetic field in a superconductor, which is an essential feature of the phenomenon. Measurement of the light-induced Meissner effect is one of the goal of the group that I joined in Max Planck Institute for the Structure and the Dynamics of Matter. Measuring the light-induced Meissner effect is fundamental for two reasons: it's an undeniable proof that the material turns superconductive; a light-induced dynamic of the effect

has never been studied before and could give access to fascinating fundamental physics knowledge.

The final measurement setup is based on two CO_2 lasers and a Ti:Al_2O_3 oscillator and the method utilized is a standard pump probe technique. For time delays larger than few nanoseconds, the ultrafast setup becomes extremely slow. Space-requirements of long-delay stages (1 ns $\approx$ 30 cm) can be solved with some advanced electronics delay configuration, but scanning for more than few nanoseconds takes hours of measurements, which implies huge cost and energy consumption.
To face this problem I started to work on a detection setup based on a Helium-Neon continuous wave (CW) laser, used to probe a mid-infrared (MIR) pumped superconductive sample. The aim of the proposed method is to acquire time-resolved pump probe data in parallel to the built ultrafast setup. The time resolution achievable by the new detection configuration is $\sim$500 ps and it matches with the ultrafast whose time resolution lies in the nanosecond range. Furthermore acquiring a time-window of e.g. 1 ms with the continuous-wave based configuration is extremely faster than with the ultrafast one: the former requires 40 minutes to get the a good signal-to-noise ratio (SNR) value, compared to almost 6 hours of the latter.

The thesis project consists in the theoretical background, development and characterization of the continuous-wave technique, together with measurement results of the superconductivity destruction upon MIR pumping on K_3C_{60} as a final test in order to evaluate the method performance.

In the first chapter the basic principle of the magnetic field optical measurement are explained, with an overview on the magneto-optic sensing techniques, the parameters to evaluate the performance of a magnetometer and a comparison with the most recent achievement in this field. In chapter 2 a theory background on polarization rotation is delineated. Polarization rotation is the physical quantity measured to reconstruct the magnetic field. Afterwords a detailed description of the experimental setup is given with a summary of the devices tested and on the choices made to optimize the performances. Then the first characterization, made on an indium antimonide slab, is shown, together with a general overview on the achievable performance of the setup with different choices of parameters. Chapter 3 is referred to the second in-depth characterization made on a Bi:YIG sample, which is the magnetic detector implemented in the Meissner detection setup. A brief summary of this rare-earth substituted iron garnet is given. In the last chapter destruction of superconductivity results upon MIR pumping on K_3C_{60} are shown, preceded by an introduction on the materials properties and on the reason of our interest on it, and by a detailed description of the experimental setup.

Chapter 1

Optical Magnetometry - Basic Principle & State of the Art

1.1 Using the Faraday Effect to measure magnetic field

Faraday effect is the physical phenomenon responsible of rotating the polarization of an electro-magnetic wave propagating through a magnetic material. The rotation is proportional to the magnetic field vector projection along the light propagation direction [5] [6]. The magnetic field induces a birefringence in the dieletric material therefore two orthogonal light polarization components expierence different refractive indices. This leads to a phase shift between them upon propagation and, if the input light is linearly polarized, a rotation of a specific angle. The rotation angle can be written as:

$$\theta = VdB \tag{1.1}$$

where V is the Verdet constant, d is the propagation path and B is the projection of the external magnetic field along the propagation direction. The Verdet constant is the proportionality term describing the strength of the Faraday effect; it's an optical property characteristic of each material and its unit is rad/(T$\cdot$ m) [7].

Using the Faraday effect to probe magnetic field is a well-estabilished method that can be developed with different detector materials, transparent to different wavelengths, and with different time and spatial features. The central idea is to reconstruct the field from the polarization rotation sensing as shown in figure 1.1. One can measure a magnetic field with a CW laser, as investigated with this thesis

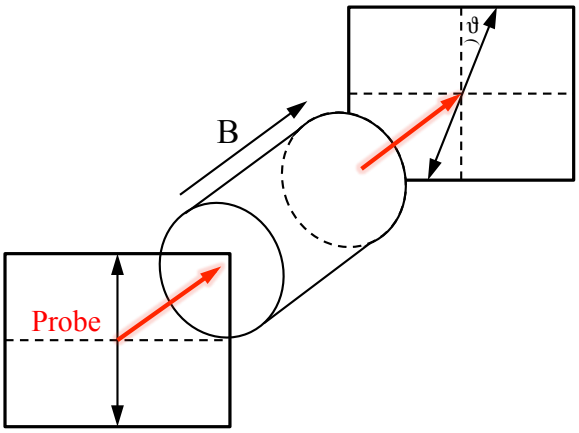

Figure 1.1: Faraday rotation scheme: the polarization of a linear polarized beam is rotated by propagation through a magnetic cylinder.

work, or with an ultrafast pulsed laser.

1.2 Present limits of optical magnetometry & Comparison with other magnetometry techniques

Nowadays magneto-optic techniques are an essential know-how in many different fields: from medical diagnostic, e.g. heart and brain biocurrents sensing [8][9], to airspace industries, detecting surface and subsurface corrosion and defects in aircrafts overlay [10]. In fundamental physics research optical magnetometry plays a crucial role. A new research frontier on superconductivity physics is due to optics related experiments which allowed for example to literally visualize magnetic flux vortices in type II superconductors or study the penetration depth of supercurrents [11][12].

Magneto-optic effect refers to the interaction between light and a material with magnetic properties. Above all, Faraday effect stands out, discovered by Michael Faraday in 1845, explained in detail in chapter 1.1. In 1876 John Kerr recognized a polarization rotation of light reflected from the surface of a magnet. From his observations another important magneto-optic effect was reported: the Magneto Optic Kerr Effect (MOKE), which is related to subatomics layer magnetism and

is now essential in low dimensional physics research [13]. In the end, Zeeman effect [14], Voigt effect and Cotton-Mouton effect [15] are worth to be reported for their lately application in magneto-optic experiments [16]. In the last two decades the commercial technology electronics related has been moving towards smaller and smaller length, down to atomic level. The well-established magnetometry workframe, based on vibrating sample magnetometer (VSM) and superconducting quantum interference devices (SQUID), is losing effectiveness, together with its cryo-temperature working regime which makes it complicated to use in specific conditions e.g. with biological samples. These are just few reasons why optical magnetometry is gaining popularity. Moreover huge magneto-optic effects have been found in many materials, such as rare-earth element doped iron garnets (see chapter 3) and magnetic alloy films, among with new discoveries on 2D materials whose magneto-optic properties can be engineered obtaining giant magnetic response [17].

Three fundamental features of a magnetometer are sensitivity, space resolution and time resolution. Different experimental aims require different values of these three essential parameters.

The ultimate bounds on sensitivity of an optical magnetometry technique are related two fundamental quantum limits i.e. projection noise and photon shot noise. Projection noise results from the angular-momentum projection of a polarized atom along an orthogonal direction which gives a random results (e.g. $\pm 1/2$) and translates into a primary noise depending on $1/\sqrt{\mathrm{N}}$ with N the number of atoms in the system. Polarization noise is characteristic of magnetometer based on atomic ensemble e.g. atomic magnetometry whose resonant medium is an alkali atoms vapour [18]. The second ultimate limit on the sensitivity is the photon shot noise, which affects the method explained in this thesis work and that is treated in detail in chapter 2.4. In general photon shot noise and polarization noise are comparable and can be reduced exploiting exotic states of light called squeezed-light in which photons with sub-poissonian statistics are used. The latter solution is not trivial to implement and depends a lot on the light sources utilized in the experiment [19]. A general rule to improve the sensitivity of a magnetometer is to increase the number of photons and atoms used which leads to larger signal to noise ratio (SNR).
In 2003 Kominis et. al developed a new magnetometry technique based on a spin-exchange relaxation-free (SERF) atomic magnetometer, demonstrating a magnetic field sensitivity of 0.54 $\mathrm{fT}/\sqrt{\mathrm{Hz}}$ with a calculated limit of 10^{-17} $\mathrm{T}/\sqrt{\mathrm{Hz}}$ [20]. This is the best resolution ever achieved. Standard SQUID and atomic magnetometers yields to sensitivity between $\mathrm{nT}/\sqrt{\mathrm{Hz}}$ to tens of $\mathrm{fT}/\sqrt{\mathrm{Hz}}$

Space resolution is determined by the size of the optical probe used by the magnetometer and can be crucial in fundamental physics measurements e.g. supercurrent flux visualization with ∼100 nm size.

Eventually time resolution is an important feature which strongly depends on the purpose of the measurement. For biological sensing in general the issue is to have a wide dynamic range from Hz to kHz with focus on the low frequency spectrum. For spin oriented experiments or Meissner effect dynamics purposes an ultrafast time-resolution is needed.
The state-of-the-art method for ultrafast magneto-optic sensing is the pump probe technique which can lead to subfemtosecond time resolution and with many different possible purposes. Indeed defining the probe pulse in a different spectrum range, from far-infrared to ultraviolet and x-rays, one chooses the transitions behind the interaction to investigate, ending up with different information [21]. The main problem of the ultrafast configurations is the complicated setup necessary, with a laser to generate short pulses, usually pretty intense, and with a space-requiring delay line.

In general magneto-optic magnetometers with large time-dynamics, i.e. their time resolution span from ultrafast timescales to milliseconds, have not been developed yet. In this ambience the new sub-nanoseconds continuous-wave laser magneto-optic probing method ranks. The space resolution needed for the aim of the light-induced Meissner effect sensing is 50 μm, to match the ultrafast probe which runs in parallel. We managed to have a beam diameter of ∼35 μm at the sample position. The magnitude of a possible signal from the mentioned experiment is not clear. Theoretically a sensitivity smaller than 1 $\mu\mathrm{T}/\sqrt{\mathrm{Hz}}$ could be enough to see a reliable signal. In practice it's very likely that a $n\mathrm{T}/\sqrt{\mathrm{Hz}}$ regime should be reached.

Chapter 2

Magneto-optic Measurement with a CW Laser

2.1 Theory of polarization rotation measurement in the presence of noise

2.1.1 Overview on polarization of light

When the direction of the electric field of light oscillates in a regular and predictable way, we can say that light is polarized. Polarization of light describes the direction of the electric field oscillations: if it oscillates in a plane, light is linearly polarized. If the electric field spiral around we say that light is circular or elliptical polarized [22]. Jones' algebra is the mathematical formalism used to describe analytically polarization of light[1]. In the next paragraph I will summarize some of Jones formalism milestones to give a insight on the problems I faced during the development of the magneto-optic sensing setup.

Let us start from the plane-wave solution to Maxwell's equations:

$$\mathbf{E}(\mathbf{r},t) = \mathbf{E}_0 e^{i(\mathbf{k}\cdot\mathbf{r}-\omega t)} \tag{2.1}$$

[1]Jones formalism is appropriate only for describing perfectly polarized light. In case of unpolarized light or partially polarized light, Mueller matrices are used.

The wave vector **k** describes the propagation direction and, neglecting absorption so that the refractive index is real, we can write it as

$$k = \frac{n\omega}{c} = \frac{2\pi n}{\lambda} \tag{2.2}$$

The only boundary condition on $\mathbf{E}_0$ is that it must be perpendicular to **k**, which means that on the other two axis $\mathbf{E}_0$ doesn't have boundaries. If we orient a reference frame with the z-axis along **k** direction we can write 2.2 as

$$\mathbf{E}(z,t) = (E_{\mathrm{x}}\hat{\mathbf{x}} + E_{\mathrm{y}}\hat{\mathbf{y}})e^{i(kz-\omega t)} \tag{2.3}$$

The relationship between $\mathrm{E_x}$ and $\mathrm{E_y}$ describes the polarization of light. If $\mathrm{E_y}$ is zero, we say that the wave is linearly polarized, and more in general a plane-wave can be said to be linearly polarized only if $\mathrm{E_x}$ and $\mathrm{E_y}$ have the same complex phase or a phase-difference of integer multiples of π. If the field never goes to zero in both dimensions it is said to be circularly or elliptically polarized.

In order to introduce the Jones vectors to describe polarization we can explicitely write the complex phases of the electric fields in x and y directions starting from equation 2.3

$$\mathbf{E}(z,t) = (|E_{\mathrm{x}}|e^{i\phi_{\mathrm{x}}}\hat{\mathbf{x}} + |E_{\mathrm{y}}|e^{i\phi_{\mathrm{y}}}\hat{\mathbf{y}})e^{i(kz-\omega t)} \tag{2.4}$$

and then

$$\mathbf{E}(z,t) = E_{\mathrm{eff}}(A\hat{\mathbf{x}} + Be^{i\delta}\hat{\mathbf{y}})e^{i(kz-\omega t)} \tag{2.5}$$

with

$$E_{\mathrm{eff}} = \sqrt{|E_{\mathrm{x}}|^2 + |E_{\mathrm{y}}|^2}e^{i\phi_{\mathrm{x}}} \tag{2.6}$$

$$A = \frac{|E_{\mathrm{x}}|}{\sqrt{|E_{\mathrm{x}}|^2 + |E_{\mathrm{y}}|^2}} \tag{2.7}$$

$$B = \frac{|E_{\mathrm{y}}|}{\sqrt{|E_{\mathrm{x}}|^2 + |E_{\mathrm{y}}|^2}} \tag{2.8}$$

$$\delta = \phi_{\mathrm{x}} - \phi_{\mathrm{y}} \tag{2.9}$$

The field $\mathrm{E_{eff}}$ is often unimportant in the polarization analysis since it represents the strength of an effective linearly polarized field and matters only in the intensity calculations. Its phase is a global phase shift that can be physically adjust moving the light source backward of forward by a fraction of a wavelength. The information about polarization are stored in equation 2.5. We refer to it as a Jones vector

and we can write it as a column vector useful in the matrix algebra in the Jones formalism:

$$\begin{bmatrix} A \\ Be^{i\delta} \end{bmatrix} \tag{2.10}$$

This vector describes the polarization state of any plane wave field. Here I summarize the Jones vectors for several polarization states:

Linearly polarized along x	$\begin{bmatrix} 1 \\ 0 \end{bmatrix}$
Linearly polarized along y	$\begin{bmatrix} 0 \\ 1 \end{bmatrix}$
Linearly polarized at angle α measured from x-axis	$\begin{bmatrix} \cos\alpha \\ \sin\alpha \end{bmatrix}$
Right circularly polarized	$\frac{1}{\sqrt{2}}\begin{bmatrix} 1 \\ -i \end{bmatrix}$
Left circularly polarized	$\frac{1}{\sqrt{2}}\begin{bmatrix} 1 \\ i \end{bmatrix}$

Table 2.1: Jones vectors for the most common polarization states.

Polarization of light can be manipulated with polarization optics i.e. polarizers and wave plates.
A linear polarizer is an optical element which lets pass only light polarized along a particular axis. It can be represented, in the Jones formalism theoretical framework,

with a square matrix and it can be applied to the input polarization state to predict what will be the effect of that element on the light [23]. For example we can represent a polarizer with transmission along the x-axis as

$$\begin{bmatrix} 1 & 0 \\ 0 & 0 \end{bmatrix} \tag{2.11}$$

and as expected, applied on a arbitrary Jones vector 2.10, it lets pass only the x-axis component:

$$\begin{bmatrix} 1 & 0 \\ 0 & 0 \end{bmatrix} \begin{bmatrix} A \\ Be^{i\delta} \end{bmatrix} = \begin{bmatrix} A \\ 0 \end{bmatrix} \tag{2.12}$$

We can schematize a general situation by

$$\begin{bmatrix} A' \\ B' \end{bmatrix} = \mathbf{J}_{\text{system}} \begin{bmatrix} A \\ Be^{i\delta} \end{bmatrix} \tag{2.13}$$

in which $\mathbf{J}_{\text{system}}$ represents the Jones matrix describing the polarization device which the light is passing through. $\mathbf{J}_{\text{system}}$ can also group a series of devices and can be calculated as

$$\mathbf{J}_{\text{system}} = \mathbf{J}_{\text{N}}\mathbf{J}_{\text{N-1}} \cdots \mathbf{J}_2\mathbf{J}_1 \tag{2.14}$$

where $\mathbf{J}_{\text{N}}$ is the n^{th} polarizing element along the system.

It's interesting to notice that one can renormalize the final Jones vector writing it in the standard form as

$$\begin{bmatrix} \tilde{A}' \\ \tilde{B}' \end{bmatrix} = \frac{e^{i\phi_{\text{A'}}}}{\sqrt{|A'|^2 + |B'|^2}} \begin{bmatrix} |A'| \\ |B|e^{i\delta'} \end{bmatrix} \tag{2.15}$$

In equation 2.15 the δ' represents the phase difference between B' and A' i.e. between the two light polarization components, which can be phase-shifted by the system. This is exactly what should be taken under control in the development of a new optical setup sensitive to polarization rotation.

2.1.2 Polarization effect of reflection

When light encounter a material interface, the amount of reflected and transmitted light depends on the impinging light polarization. The ratio of reflected and transmitted field components are given by the Fresnel coefficient

$$r_{\text{s}} = \frac{E_{\text{s}}{}^{(\text{r})}}{E_{\text{s}}{}^{(\text{i})}} = \frac{n_{\text{i}} \cos\theta_{\text{i}} - n_{\text{t}} \cos\theta_{\text{t}}}{n_{\text{i}} \cos\theta_{\text{i}} + n_{\text{t}} \cos\theta_{\text{t}}} \tag{2.16}$$

Linear polarizer	$\begin{bmatrix} \cos\theta^2 & \sin\theta\cos\theta \\ \sin\theta\cos\theta & \sin\theta^2 \end{bmatrix}$
Half wave plate	$\begin{bmatrix} \cos 2\theta & \sin 2\theta \\ \sin 2\theta & -\cos 2\theta \end{bmatrix}$
Quarter wave plate	$\begin{bmatrix} \cos\theta^2 + i\sin\theta^2 & (1-i)\sin\theta\cos\theta \\ (1-i)\sin\theta\cos\theta & \sin\theta^2 + i\cos\theta^2 \end{bmatrix}$
Reflection from an interface	$\begin{bmatrix} -r_\mathrm{p} & 0 \\ 0 & r_\mathrm{s} \end{bmatrix}$
Transmission through an interface	$\begin{bmatrix} t_\mathrm{p} & 0 \\ 0 & t_\mathrm{s} \end{bmatrix}$
Rotator i.e. Faraday rotator	$\begin{bmatrix} \cos\theta & \sin\theta \\ -\sin\theta & \cos\theta \end{bmatrix}$

Table 2.2: Common Jones Matrices. θ is measured with respect to x-axis and specifies the transmission axis of a linear polarizer or the fast axis of a wave plate.

$$t_\mathrm{s} = \frac{{E_\mathrm{s}}^{(\mathrm{t})}}{{E_\mathrm{s}}^{(\mathrm{i})}} = \frac{2n_\mathrm{i}\cos\theta_\mathrm{i}}{n_\mathrm{i}\cos\theta_\mathrm{i} + n_\mathrm{t}\cos\theta_\mathrm{t}} \tag{2.17}$$

$$r_\mathrm{p} = \frac{{E_\mathrm{p}}^{(\mathrm{r})}}{{E_\mathrm{p}}^{(\mathrm{i})}} = \frac{n_\mathrm{i}\cos\theta_\mathrm{t} - n_\mathrm{t}\cos\theta_\mathrm{i}}{n_\mathrm{i}\cos\theta_\mathrm{t} + n_\mathrm{t}\cos\theta_\mathrm{i}} \tag{2.18}$$

$$t = \frac{{E_\mathrm{p}}^{(\mathrm{t})}}{{E_\mathrm{p}}^{(\mathrm{i})}} = \frac{2n_\mathrm{i}\cos\theta_\mathrm{i}}{n_\mathrm{i}\cos\theta_\mathrm{t} + n_\mathrm{t}\cos\theta_\mathrm{i}} \tag{2.19}$$

with reference to figure 2.1, defining $\mathrm{E_s}$ and $\mathrm{E_p}$ as the electric field components

respectively perpendicular and parallel to the incidence plane [24]. These represent the polarization components of the field in a system of reference relative to the incidence plane.

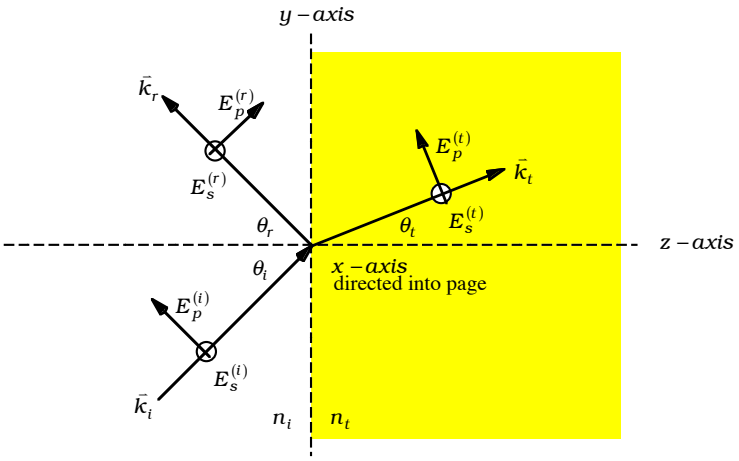

Figure 2.1: Incident, reflected and transmitted plane wave fields at a material interface. Adapted from [22].

The incident and transmitted angle obey the Snell's law.

$$n_{\mathrm{i}} \sin\theta_{\mathrm{i}} = n_{\mathrm{t}} \sin\theta_{\mathrm{t}} \tag{2.20}$$

Using Jones algebra, as shown already in table 2.2, the matrix corresponding to a reflection from a surface is

$$\begin{bmatrix} -r_{\mathrm{p}} & 0 \\ 0 & r_{\mathrm{s}} \end{bmatrix} \tag{2.21}$$

and to a transmission through a material is

$$\begin{bmatrix} t_{\mathrm{p}} & 0 \\ 0 & t_{\mathrm{s}} \end{bmatrix} \tag{2.22}$$

Let us focus on the reflection case from a metallic surface for the purpose of this thesis work[2]. Potentially, if the incidence plane is tilted of an angle θ e.g. a mirror

[2]In case of reflection from a dielectric mirror the situation is similar but with transmission from a denser medium to air or vacuum.

is vertically tilted, we must reorient the coordinate system multiplying the incident Jones vector by the Jones matrix for a rotator:

$$\begin{bmatrix} \cos\theta & \sin\theta \\ -\sin\theta & \cos\theta \end{bmatrix} \tag{2.23}$$

Let us define $N = n_t/n_i$ and using the Snell's law we can rewrite the sin of the transmitted angle as

$$\sin\theta_{\mathrm{t}} = \frac{\sin\theta_{\mathrm{i}}}{N} \tag{2.24}$$

It is crucial to point out that the complex nature of N doesn't affect our calculation so far.

The cosine of θ_{t} can be written as

$$\cos\theta_{\mathrm{t}} = \frac{\sqrt{N^2 - \sin\theta_{\mathrm{i}}{}^2}}{N} \tag{2.25}$$

Upon substitution in 2.16 and 2.18 we rewrite the Fresnel reflection coefficient as function of the angle of incidence θ_{i}

$$r_{\mathrm{s}} = \frac{\cos\theta_{\mathrm{i}} - \sqrt{N^2 - \sin\theta_{\mathrm{i}}{}^2}}{\cos\theta_{\mathrm{i}} + \sqrt{N^2 - \sin\theta_{\mathrm{i}}{}^2}} \tag{2.26}$$

$$r_{\mathrm{p}} = \frac{\sqrt{N^2 - \sin\theta_{\mathrm{i}}{}^2} - N^2\cos\theta_{\mathrm{i}}}{\sqrt{N^2 - \sin\theta_{\mathrm{i}}{}^2} + N^2\cos\theta_{\mathrm{i}}} \tag{2.27}$$

These expression can be placed into the Jones matrix 2.21 to evaluate the effect on polarization but it looks clearer if we explicitly consider the refractive index as a complex number and rewrite 2.26 and 2.27 as

$$r_{\mathrm{s}} = |r_{\mathrm{s}}|e^{i\delta_{\mathrm{r_s}}} \tag{2.28}$$

$$r_{\mathrm{p}} = |r_{\mathrm{p}}|e^{i\delta_{\mathrm{r_p}}} \tag{2.29}$$

Even if the reflectivity is on the order of unity, e.g. for a reflection from a metallic mirror, the phases upon reflection can be very different for the two polarization components because $\delta_{\mathrm{r_p}}$ and $\delta_{\mathrm{r_s}}$ are different, depending on the incidence angle θ_{i}. If the input light has only one polarization components, i.e. it is represented

by Jones vectors $\begin{bmatrix}1\\0\end{bmatrix}$ or $\begin{bmatrix}0\\1\end{bmatrix}$, nothing happens and the polarization is maintained. When the input polarization has both s and p component a reflection from a metal surface adds a phase shift between them altering the input polarization state which becomes elliptical.
For the purpose of the experiment a Faraday rotation is induced such that the light impinging on the mirrors after the sample position has both s and p components.

$$\begin{bmatrix}1\\0\end{bmatrix} \cdot \begin{bmatrix}\cos\theta & \sin\theta\\ -\sin\theta & \cos\theta\end{bmatrix} = \begin{bmatrix}\cos\theta\\ -\sin\theta\end{bmatrix} \tag{2.30}$$

Then the reflection from a metallic mirror can be taken into account multiplying the input vector to a retarder matrix with η defining the retardation between polarization components:

$$\begin{bmatrix}\cos\theta\\ -\sin\theta\end{bmatrix} \cdot \begin{bmatrix}-r_{\mathrm{p}} & 0\\ 0 & r_{\mathrm{s}}\end{bmatrix} = \begin{bmatrix}e^{-\frac{i\eta}{2}}\cos\theta\\ -e^{\frac{i\eta}{2}}\sin\theta\end{bmatrix} \tag{2.31}$$

The higher is the angle of incidence of the input light, the larger is this phase shift so the more elliptical becomes the initial polarization state. An angle fluctuation around a small angle of incidence yields to an ellipticity much lower than a fluctuation around a higher angle. This is the reason behind a quasi-zero-degrees mirrors choice in an optical setup sensitive to polarization.

2.1.3 Setup description

The purpose of the setup I built is the a magnetic field measurement, sensing the polarization rotation of a linearly polarized laser due to the Faraday effect induced by the field in an high Verdet constant material.

In figure 2.2 a schematic of the setup is shown. A probe beam is generated by a continuous wave laser with frequency ∼633 nm. The polarizer guarantees a linear polarization of the input light. The probe-beam is then focused onto the sample by a plano-convex lens. The reflected beam is collected by the same lens and collimated. It proceeds consecutively through a half-wave plate and a Wollaston prism. The latter separates the two polarization component s and p of the light, which are then collected by two mirrors and redirected onto a balanced photodetector. The balance photodetector output signal is the difference between the power sensed on the two photodiodes. This signal is then processed by an oscilloscope triggered with the pump pulse arrival and saved.
The half-wave plate is necessary to add a phase shift to the probe in order to

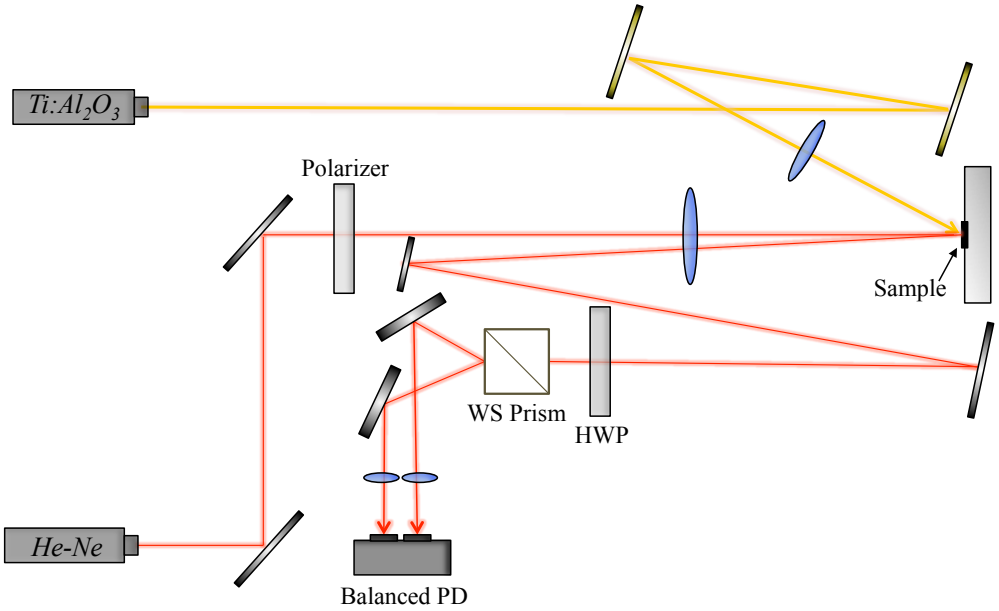

Figure 2.2: Scheme of the magneto-optic measurement with a CW laser setup. The red lines represent the CW probe laser; the yellow lines represent the Ti:Sapphire pump beam. Blue ellipses stand for optical lenses while yellow and grey narrow rectangles for gold and silver uncoated mirrors respectively. All other components are labelled.

have a balanced signal in the unperturbed situation, balancing for example for not-light-induced birefringence or polarization noise in the beam line. In other words when the pump is turned off the two polarization components should carry the same amount of power onto the two photodiodes. In this way when the pump shines the sample, the induced polarization rotation becomes evident. The sample is pumped with a femtosecond near-infrared pulsed generated with a Ti:Al_2O_3 laser.

This configuration is optimized to reduce the polarization noise introduced by different optical elements in the scheme: propagation through not-perfect wave plates and reflection from metallic mirrors.
In particular, as explained in chapter 2.1.2, a reflection from a metal surface, or from a dielectric mirror, introduces an ellipticity to the input polarization state if it's not perfectly vertical or horizontal. This effect can be dramatically reduced if the angle of incidence with the mirror is close to zero. In figure 2.3 two different configurations are shown: in panel (a) the angle of incidence is around 22.5°, while in panel (b) all the mirrors are quasi-zero-degree incidence angle, which means

that the induced ellipticity is minimum. In itself the ellipticity can degrades the polarization rotation signal but can be compensated e.g. with a wave plate. The problem is that each pointing fluctuation, i.e. tiny movement of the laser beam, due to instability of the optics or of the laser itself, leads to a different angle of incidence on the mirror which translates in noise in the polarization rotation signal. At first we started with configuration (b). After placing a polarizer right before the Wollastone Prism to cut off every polarization noise due to the explained mechanism, we found out that the noise level was an order of magnitude lower (from $\sim 20\,\mu\text{Rad}/\sqrt{\text{Hz}}$ to $1\ \mu\text{Rad}/\sqrt{\text{Hz}}$). This convinced us to change the setup configuration heading to the final scheme shown in figure 2.2.

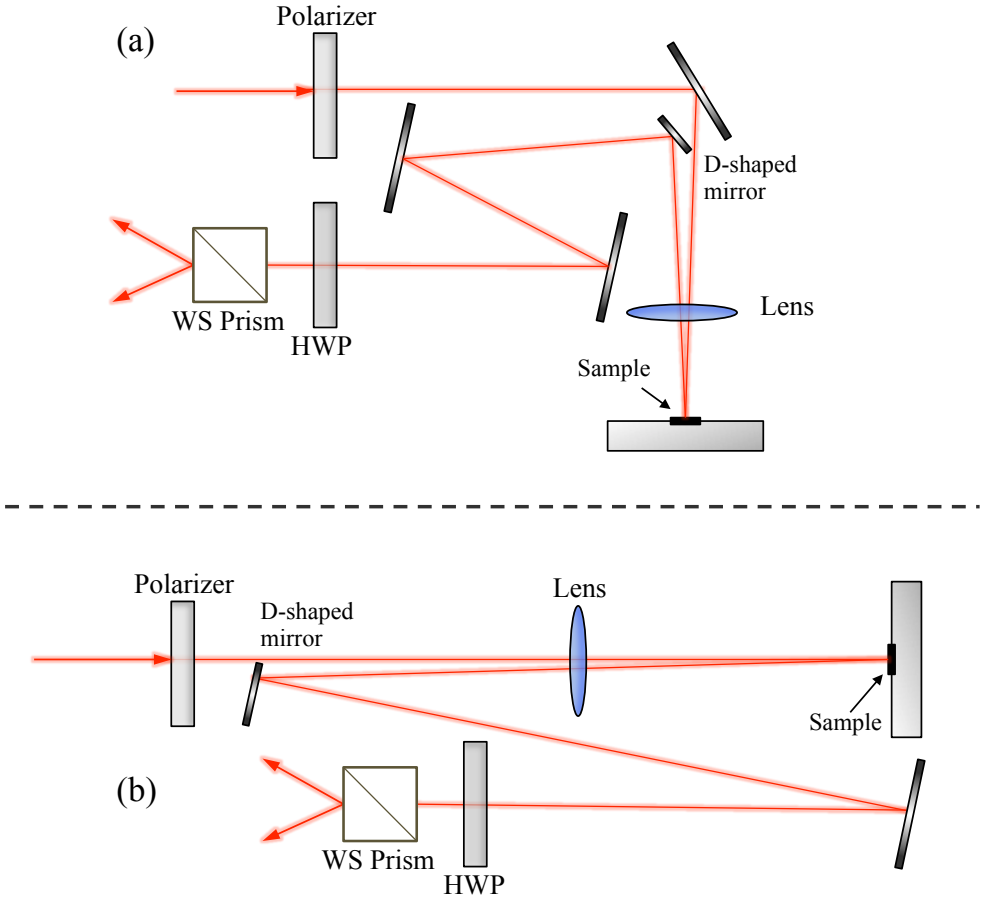

Figure 2.3: (a) Setup scheme with 45° mirrors which leads to high polarization noise. (b) Setup scheme with quasi-zero-degrees mirror with minimum polarization noise.Red lines represent the CW probe laser.

2.2 Characterization of the setup

Building the setup requires to decide which optical components are more suitable for the purpose I want to achieve, with different features depending on the type of measurement it is wanted e.g. different time resolutions need balanced photodetectors with a different bandwidth; higher sensitivity requires more stable laser, etc.

Three continuous wave laser have been tried. As shown in table 2.3 and in figure 2.4, each of them have different noise performance and polarization ratio. The stabilized Helium Neon laser by Thorlabs is ultimately the best in terms of noise at the expense of lower power, that is a key factor in the sub-nanosecond detection. This statement is made with reference to results shown in section 2.4.

Laser	λ	**Power**	**Polarization Ratio**	$1/e^2$ **Beam Diameter**
Thorlabs He-Ne	632.8 nm	5 mW	500:1	0.81 mm
Ultra Low-Noise Coherent Diode Module	635 nm	5 mW	Not specified	1 mm
Thorlabs stabilized He-Ne	632.99 nm	1.2 mW	1000:1	0.65 mm

Table 2.3: CW Laser specifications.

In table 2.4 balanced photodetectors' specifications are shown. The signal of interest is the difference between the voltage signal detected by two separated photodiodes. This difference is amplified. The gain–bandwidth product (GBWP) for the detector is the product of the detector's bandwidth and the gain at which the bandwidth is measured [25]. The GBWP is constant, which implies that the higher is the bandwidth, the lower is the gain.
We managed to utilize a sophisticated ultrafast balanced photodetector with bandwidth of $\sim$1.5 GHz. The main issue related to this device is the gain which is very low, resulting in small signals often buried into noise. Nevertheless the time performance of this detector are noteworthy, as shown in figure 2.5.

In the end a fiber coupling of the probe light has been carried out into a single mode optical fiber. The grounds of this choice are multiple: the spatial stability of the single-mode fiber output light which is smooth, relatively not noisy and

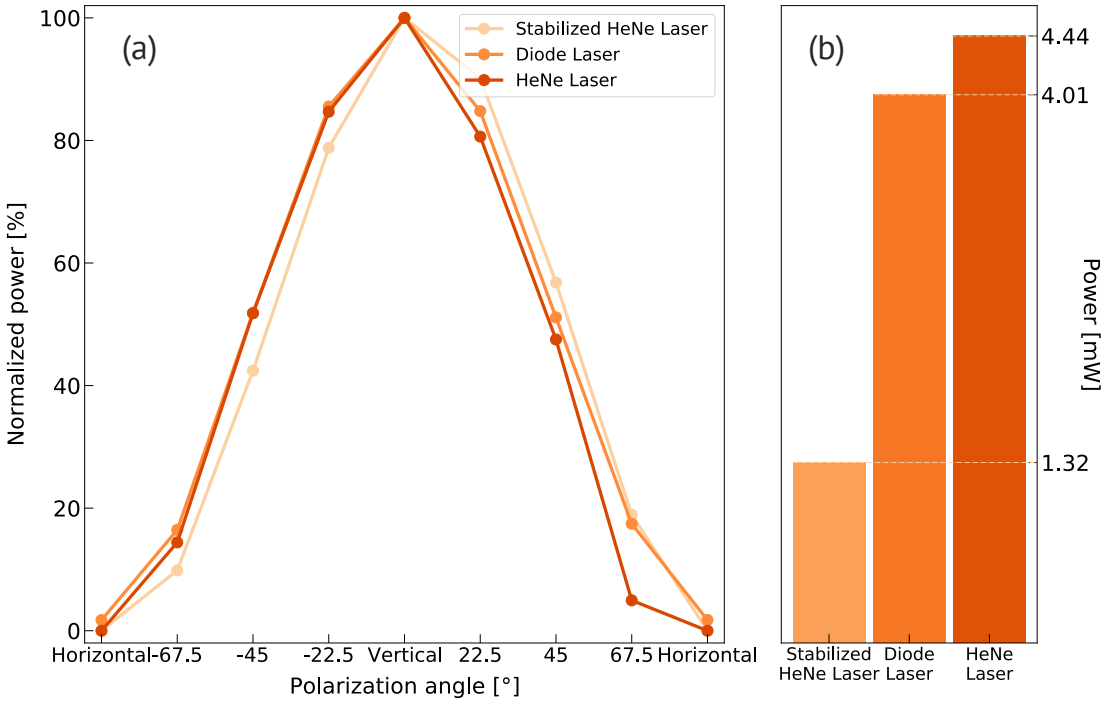

Figure 2.4: **(a)** Polarization characterization of the three continuous-wave lasers tested. **(b)** CW Lasers power comparison.

which can be easily telescoped and collimated with a specific output collimator to a desired beam diameter; the versatility of an optical fiber that can be placed handily in a already-built setup with limited space, as the case of the Meissner effect detection setup described in chapter 4.

Specifically a polarization maintaining fiber has been employed with a coupling efficiency of 75% with reference to the 5 mW Helium-Neon laser and with 60% polarization ratio compared to the input light. A single-mode fiber has been also tried but discarded for poor polarization behaviour: polarization ratio at the output of 25% compared to the input of the laser.

Detector	Bandwidth	Gain	Detector diameter
2007 Nirvana Auto-Balanced Optical Receiver, Newport	125 kHz	$5.2 \cdot 10^5$ V/W	2.5 mm
PDB410A, Thorlabs	100 MHz	$26.5 \cdot 10^3$ V/W	0.8 mm
Ultrafast balanced detector GHz-Series GDP183, Ultrafast sensors	1.5 GHz	106 V/W	0.3 mm

Table 2.4: Specifications of the balanced photodetectors tested and used.

2.3 Data acquisition

Data acquisition plays a key role in the continuous wave probing because of the large amount of data processed for a single acquisition. Compared with the standard ultrafast pump-probe technique, the amount of data acquired with the proposed method is much higher because for each acquisition a full time trace is acquired and, depending on the time resolution and on the total acquisition time, millions of data points are stored. Thus the acquisition protocol should be optimized both in time and memory.

2.3.1 DAQ Hardware and protocol

Data acquisition is performed by an oscilloscope. Three oscilloscopes has been tried as shown in table 2.5.

Oscilloscope	Bandwidth	Max Sample Rate
PicoScope 4262	5 MHz	10 MS/s
PicoScope 5444	200 MHz	1 GS/s
Tektronix MSO46	1.5 GHz	250 GS/s

Table 2.5: Oscilloscopes' Specifications.

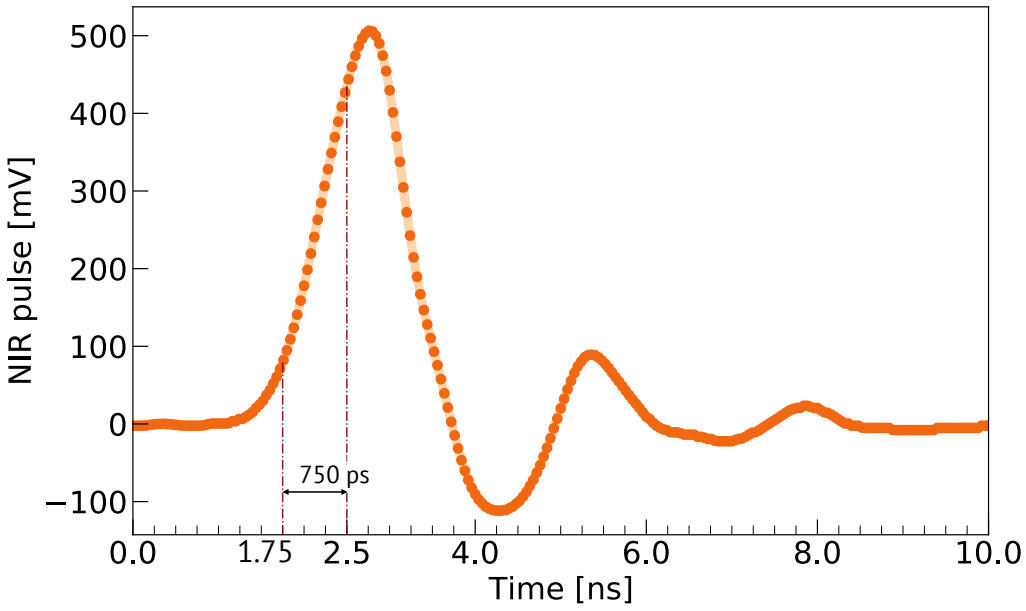

Figure 2.5: Ultrafast balanced photodetector time performance: measure of a 35 fs pulse generated by a Ti:Al_2O_3 laser and directed into one of the two photodiodes. The measurement has been taken collectively with a 1.5 GHz oscilloscope.

To maximize the SNR of the measurement a certain number of figures have to be taken and averaged. This acquisition operation is not trivial and is divided in two steps:

- The oscilloscope performs an internal average of sequential waveforms. Basically each trigger event corresponds to an acquired waveform that is averaged with the previous acquisitions. After n events the waveform saved in the oscilloscope memory is the n-average of the waveform of interest. Ideally the oscilloscope doesn't lose any trigger, thus the acquisition is optimum. In reality there is a discrepancy between calculated acquisition time and effective due to some oscilloscope internal electronics delay, especially for high sampling rate.

- The averaged waveform is transferred to the PC through an Ethernet cable and saved into a database with its own time-stamp, useful for reconstruction of the experimental condition during the acquisition.

This two operations are repeated m times. Yet the m-waveforms are averaged providing the ultimate measure i.e. $m \cdot n$ averages.
All the operations are run and controlled by a software written on purpose. The code is written in python and works with the pyVisa library which allows to open a communication with the oscilloscope creating a distinct oscilloscope class.
To summarize the acquisition process: measurement parameters are set; acquisition is started; waveforms are acquired and transferred $m \cdot n$ times; the data are converted from binary to meaningful voltage values and saved on the PC.

This is a general overview on the acquisition process. The codes are slightly different for the different oscilloscopes, as well as the time performance.

2.3.2 Acquisition-time Analysis

All the acquisition-time analysis has been made with the 1.5 GHz oscilloscope since its performances are far apart from the others oscilloscopes tried and it is the device employed for most of the results shown in this experimental thesis work.

There are 3 parameters to take into account in the choice of the time framework of the measure: the sample rate, the record length i.e. the number of points acquired by the oscilloscope and the total acquired time window. These three variables are interconnected and can't be shuffled independently.

$$\text{Record Length} = \text{Sample Rate} \cdot \text{Time Window} \tag{2.32}$$

In figure 2.6 and 2.7 time acquisition data are shown with fixed sample rate at 312.5 MS/s and fixed record length at 312.5 kpts respectively. The choice of the locked parameters is related to the experimental measure of destruction of superconductivity by a MIR pulse explained in detail in chapter 4. The oscilloscope was triggered by the pump laser pulse arrival at 20 Hz. The number of averages performed internally by the device was 1000.
It is evident that, remaining in a regime of one-trigger-per-waveform, the acquisition time is optimum since it's less than 50 ms. When the acquisition time passes the two-triggers-per-waveform threshold the acquisition time increases dramatically losing up to 50% of the triggers. An analogous thing happens when the acquisition time window is large and the sample rate is increased.

Another variable that affects both the time and the sensitivity performance is

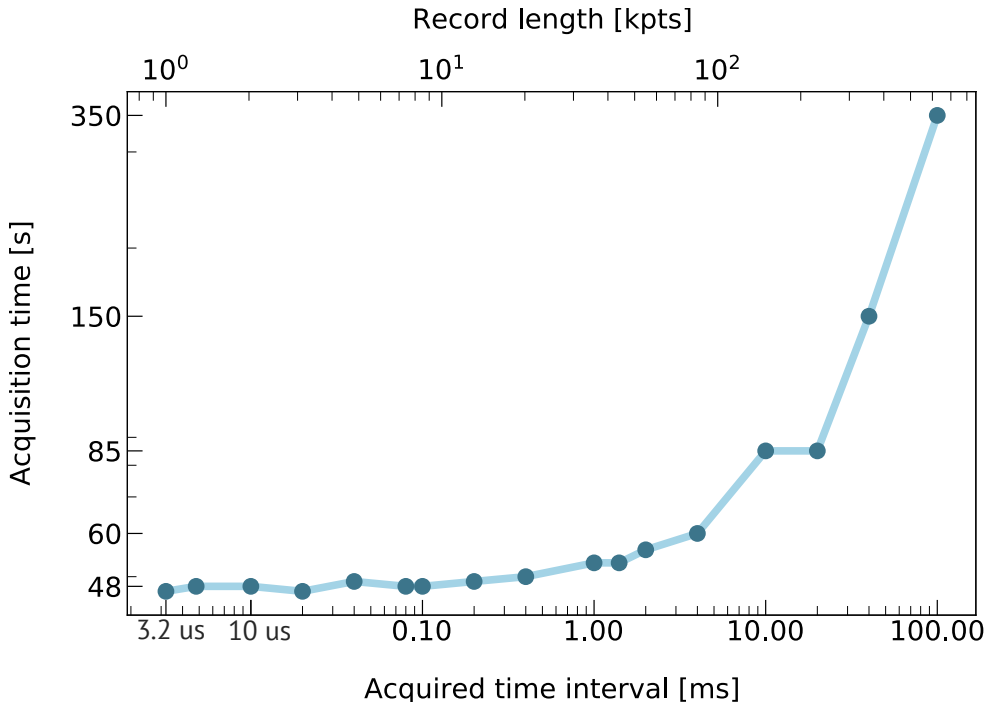

Figure 2.6: Acquisition time analysis with fixed sample rate at 312.5 MS/s.

the number of averages internally taken by the oscilloscope. In figure 2.8 can be seen that, although the acquisition time increases linearly with the number of averages, the minumum detectable angle drops dramatically before the 500 averages threshold. This is a good reason to acquire with less than 500 averages to optimize the acquisition time.

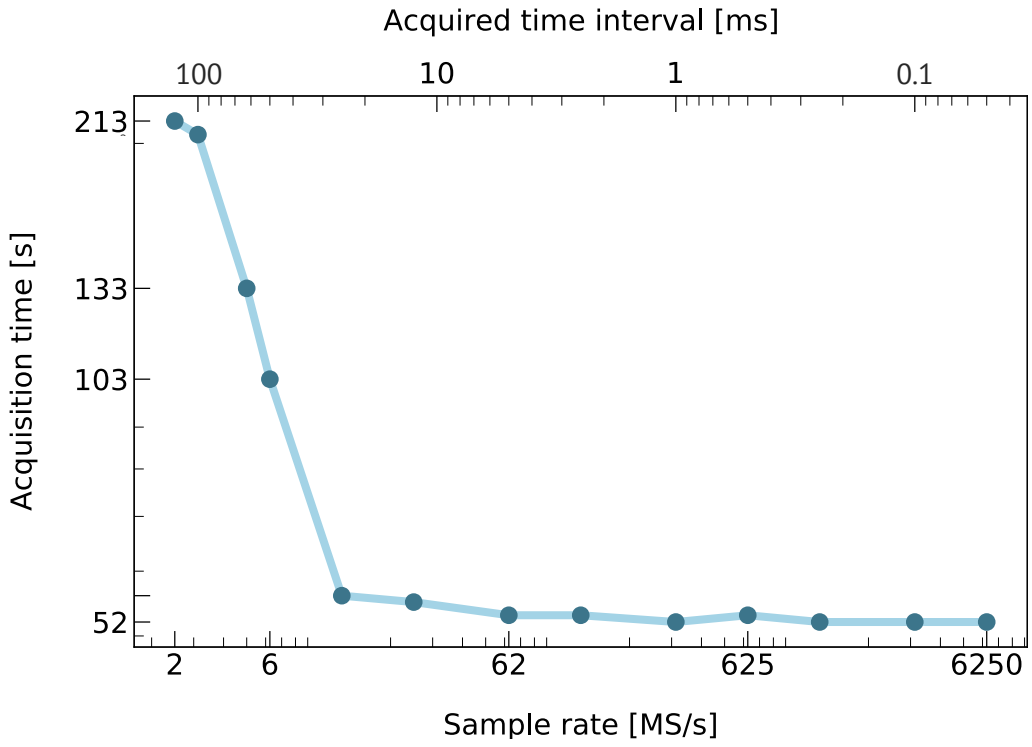

Figure 2.7: Acquisition time analysis with fixed record length at 312.5 kpts.

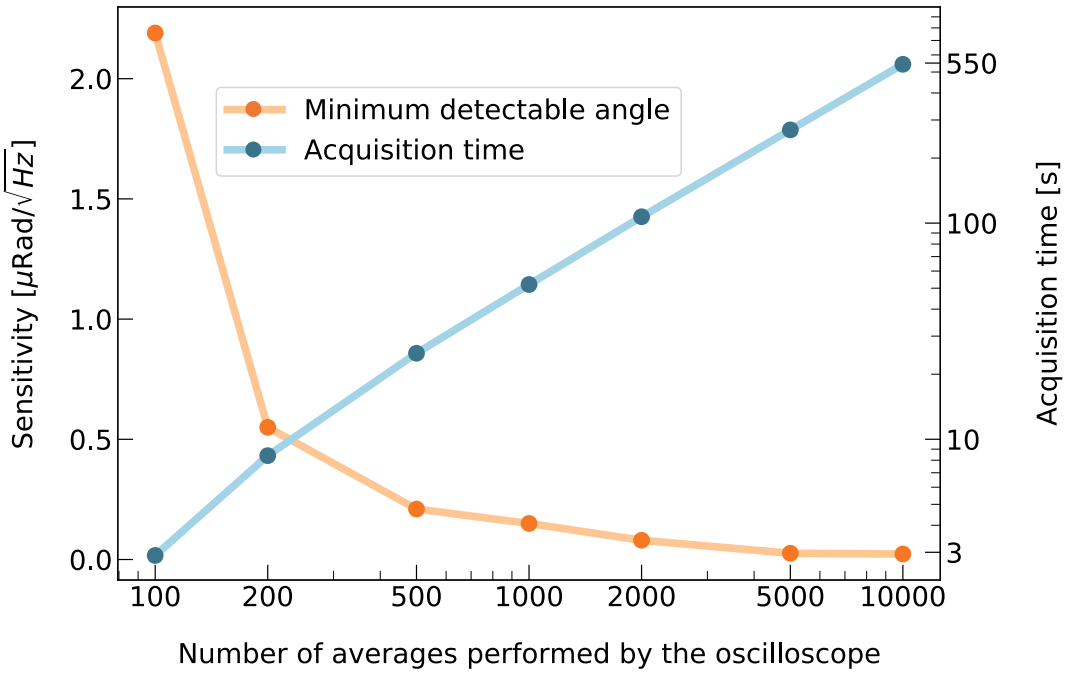

Figure 2.8: Time acquisition and sensitivity as function of the internal number of averages performed by the 1.5 GHz oscilloscope.

2.4 Achievable noise performance & remaining limits

In order to analyze and describe the sensitivity of the continuous-wave laser magneto-optic setup, a figure of merit has been defined. Given a measurement dataframe with a certain number of figures acquired, the sensitivity is defined as the mean value of the standard error of the dataset $[\mu\text{Rad}/\sqrt{Hz}]$. It corresponds to the value of an hypothetical signal such that $SNR = 1$, which means that the signal cannot be distinguished from the background noise.

As shown in figure 2.9, many different performances are achieved with different time resolution features. Peculiarly the best cases analyzed are the NIR pump-probe

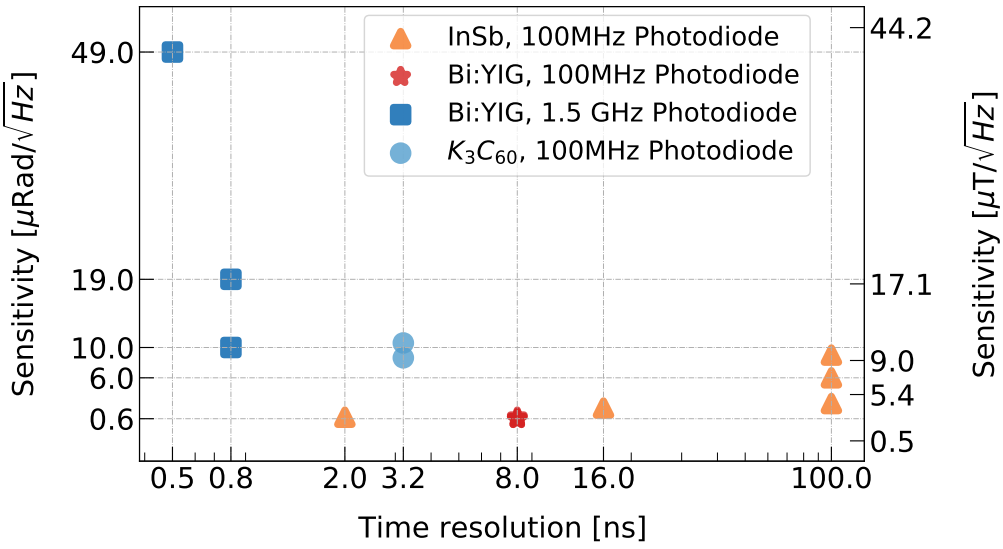

Figure 2.9: Sensitivity for different setup configuration and samples.

data on InSb slab and the Bi:YIG measurements, obtained with the 100 MHz photo-diode (see section 2.5 and 3.2).
The figure of merit in those case is $0.6\,\mu\text{Rad}/\sqrt{\text{Hz}}$. The 2 ns time resolution of the setup was obtained pushing the limit of the balance photo-detector together with the 1.5 GHz oscilloscope extreme good features. This value is really promising and it's reasonable to think that we are close to the shot-noise limit of the setup. Let us briefly estimate the shot noise contribution to compare it with our result. Shot noise is a consequence of the quantum nature of light.
Photon detection events occur independently one from each other and the statistics

describing this process is a poissonian distribution, with a certain mean value and variance. Thus the number of photon detected fluctuates with variance equal to the square root of the expected number of photons counted in that period of time [26]. Only special quantum state of light called amplitude squeezed coherent state shown a sub-poissonian distribution with fluctuation smaller than the square root of the expected number of photons, but this peculiar state are not trivial to obtain and in general are far from the possibility of this setup [27].
Let's calculate the shot noise Power Spectral Density (PSD) with reference to our setup data, i.e. 100 MHz balance photodetection and 1.5 mW He-Ne laser hitting the photodetector, as in the Meissner Effect detection configuration.

$$PSD_{\text{Shot Noise}} = GK\sqrt{\frac{P}{h\nu}}h\nu = 0.14\,\mu\text{Rad}/\sqrt{\text{Hz}} \tag{2.33}$$

G is the conversion gain of the detector [$26.5{\cdot}10^3$ V/W]; K is the calibration factor from V to Rad [0.18 Rad/V]; P is the power hitting the photodiode [W]; hν is the photon energy at 633nm. As expected, our figure of merit is very close to the shot noise limit, but we have still margin of improvement. In figure 2.10 a projection of the shot noise PSD with higher laser power is shown. This could be a net improvement for the method because increasing the overall laser power, the signal will increase linearly, differently from the shot noise contribution resulting in a higher SNR. The power increasing can be performed using a more powerful CW laser (up to 10 mW), making sure that the sample is not heated by the high power.

With the use of the ultrafast 1.5 GHz balance photo-detector a 500 ps time resolution can be reached, at the expense of sensitivity which increases of an order of magnitude at least, because of the higher noise collected by the instrument. This time resolution ideally is the regime in which we want to work but the noise performance is not sufficient for a good polarization angle detection yet.

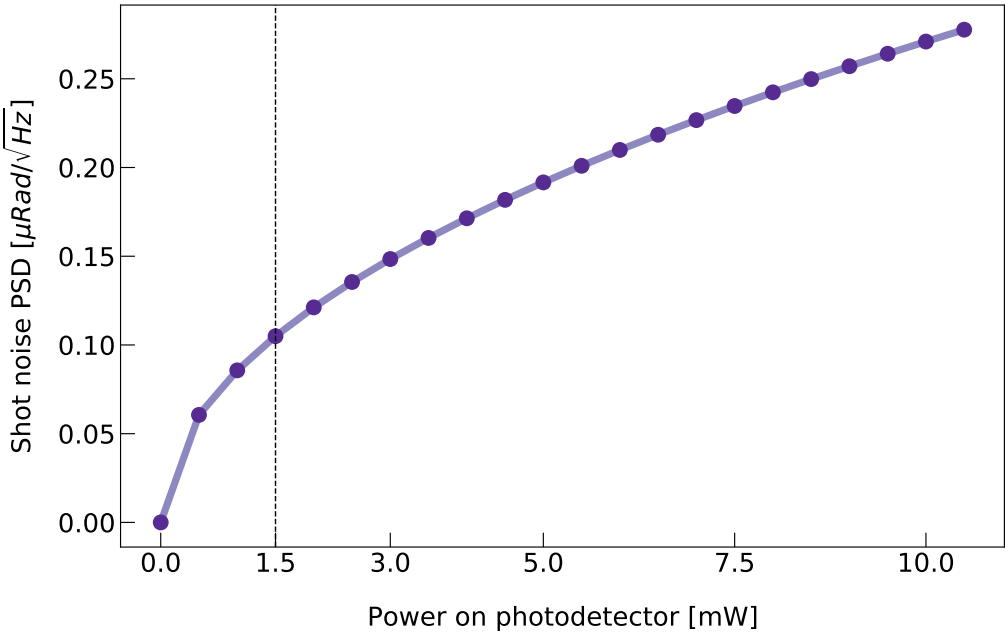

Figure 2.10: Shot noise power spectral density as function of the power hitting the photodiodes of the balance photodetector. The dashed line points out the laser power of the measurement performed.

As described in chapter 4 the detection of magnetic field on K_3C_{60} in the Meissner effect probing setup was not trivial mainly because of the small magnetic signal (1 % of the external magnetic field). In the measurement taken the signal was so small that with the low gain of the ultrafast balance photo-detector I could not recover it, buried in the noise, emphasized by the low temperature (8 K). If I forgo 500 ps time resolution for an honest 3.2 ns, compatible with the 100 MHz photo-diode, the figure of merit is around 10 μRad/$\sqrt{Hz}$. Operating with the 1.5 GHz photodiode in this low temperature regime implies a dramatic increase of the noise.

On the right y-axis of figure 2.9 the magnetic field equivalent of the polarization rotation figure of merit is shown. The conversion has been done with reference on the Bi:YIG at 633 nm Verdet constant, as explained in chapter 3.

The space resolution of the proposed detection setup is only related to the spot-size of the probe-beam on the sample. The more it is focused, the smallest is the space-resolution which means that we can detect a smaller surface of the sample each measurement i.e. we are sensitive to a smaller part of the sample. For the

test-setup (InSb and Bi:YIG) the CW laser spot-size was 1 mm FWHM.
When I implemented the CW probing system in the Meissner effect detection setup I had to reduce the beam-size a lot because its dimension would have had to be comparable with the ultrafast FWHM probe (50 μm). I obtained a FWHM of 35 μm in the sample position. In general the ultimate limit on space resolution was the detector thickness, i.e. $\sim$4 μm,

In conclusion, the main limit of the detection setup is the noise level at sub-ns time resolution. In particular, on top of the white noise characteristic of the ultrafast electronics necessary to operate in a sub-ns time regime, there is a large noise contribution due to a coupling of an external EM pulse with the instrument. The pump Ti:Al_2O_3 laser is mode-locked by two Pockels cells which couple with the 1.5 GHz detector. This contribution can be reduced until a certain minimum as can be seen in figure 2.11. This environmental electronic noise contribution is even worse in the Meissner effect detection setup where the CO_2 laser used to generate the pump pulses emits very powerful EM pulses that couple also with slower and less sensitive electronics. Even shielding the detector with a metallic cage doesn't solve this issue.On the other hand these noise elements are just part of the background and can be subtracted out.

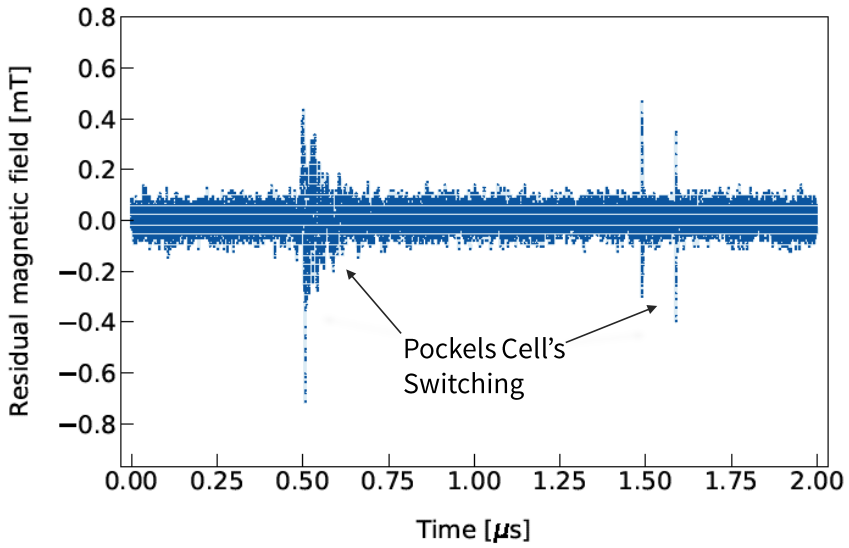

Figure 2.11: Residual detected magnetic field due to a Pockels cell coupling with the 1.5 GHz photodiode

2.5 Pump-Probe measurement on InSb

The first characterization of the setup performances has been made on a Indium Antimonide (InSb) slab. Indium Antimonide is a narrow-gap semiconductor material used in infrared detectors. I decided to use this material because, being a semiconductor, it would have manifested a pump-probe signal if excited with a NIR intense pulse.

The pump pulse was generated with a Ti:Al_2O_3 laser, 1 kHz repetition rate, 12 mJ, pulse duration of 35 fs and $1/e^2$ beam diameter 9 mm. The beam was then attenuated through a series of beam splitters (37% + 5%). With a 50 cm focal length lens I focused the pump beam onto the InSb slab obtaining a beam waist diameter, at the sample position, of 0.83 mm, measured with a knife-edge technique. In the end the fluence on the sample was 1.92 mJ/cm^2.

In figure 2.12 three pump-probe measurements on InSb are shown. The signal is relatively small and its physics is related to a change of refractive index induced by the 800 nm high-power pump pulse which rotates the polarization of the continuous wave probe, overlapped in the sample position. These measurements have been taken not to investigate on the material properties themselves rather to look at the quality of the detected signal. It's evident how the performances of the diode laser are much worse compared to the other two Helium-Neon lasers as can be seen in figure 2.13. This was the reason why I decided not to use the diode laser for further measurement.

The sensitivity obtained with the setup is 0.6 $\mu\text{Rad}/\sqrt{\text{Hz}}$ with the stabilized helium-neon laser. To be the first setup test this result was satisfying and a good starting point before moving to a magnetic field measurement.

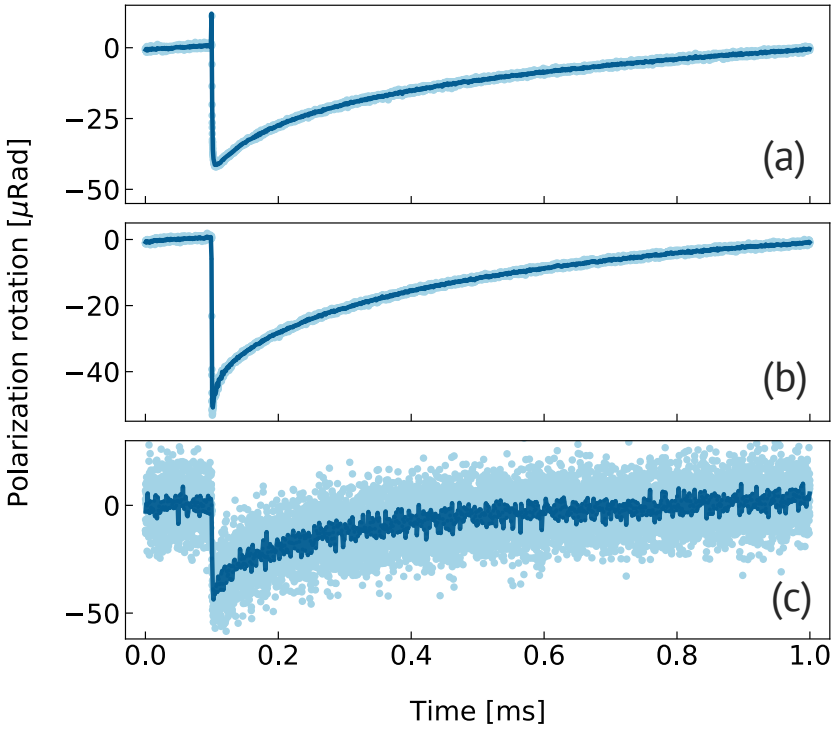

Figure 2.12: Pump-Probe signal on InSb slab pumped with a NIR pulse measured respectively with **(a)** Helium-Neon laser, 5 mW output power; **(b)** intensity stabilized Helium-Neon laser, 1.2 mW output power; **(c)** diode laser, 5 mW output power. The light-blue shade shows the whole data set, plotted to point out the difference in the variance of the acquired data.

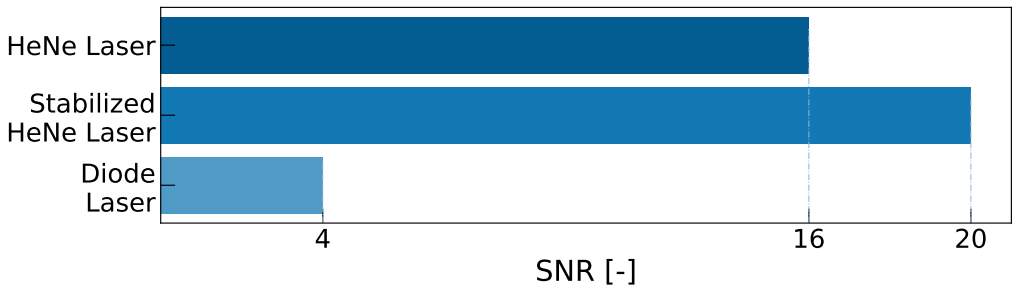

Figure 2.13: Comparison of three different lasers pump probe measurement SNR on InSb slab pumped with a NIR pulse.

Chapter 3

NIR Pump-Probe Measurement on a Ferromagnet

3.1 Bi:YIG and its use as a magneto-optic detector

In chapter 1.1 the Faraday effect as a method to detect a magnetic field has been discussed. In general the main issue of this technique is the choice of the sensing material, because of the very low Verdet constant value in most of the materials.

In the last 15 years the rare earth doped yittrium-iron garnets
R_1:$Y_2Fe_5O_{12}$ became popular because of their huge figure of merit (V larger than 1 Rad/(T$\cdot$ cm) at $\lambda = 1.5$ μm), and their transparency in the visible and infrared region [28] [29]. These two features gave it an incredible relevance in the optical-magnetometry application [30]. In particular Bismuth substituted yttrium-iron garnet Bi:YIG crystals are now a standard material for optical magnetic field sensing, and it is our choice for the magnetic detector in the light-induced Meissner effect dynamic probing experiment.

Bi_1:$Y_2Fe_5O_{12}$ is a ferromagnetic insulator with a characteristic cubic garnet crystalline structure. The out-of-plane saturation magnetic field is $\sim$ 260 mT and it's around 50 times bigger than the in-plane one [31]. The idea behind the B field detection with this material is to place the Bi:YIG into the field of interest and probe it with a laser. If the magnetic field changes, the polarization of the probe is rotated proportionally.

3.2 NIR Pump-Probe results on Bi:YIG

The characterization of the magneto-optic measurement setup was made on a wedged slab of Bi:YIG placed on a permanent magnet. The slab was pumped with a Ti:Al_2O_3, 1 kHz repetition rate, 35 fs pulses with different fluences and probed with a stabilized CW He-Ne laser (1.2 mW). The sample was wedged to avoid back reflection in the probe line and the reflected beam of interest was the second one. All the described scheme is shown in figure 3.1. The magnetic field was applied normally to the light incidence plane and its drawn is just for visualization of the field lines even though it's not quantitative. The probe beam passed through the sample twice, therefore a factor of 2 should be included in the Faraday rotation calculation.

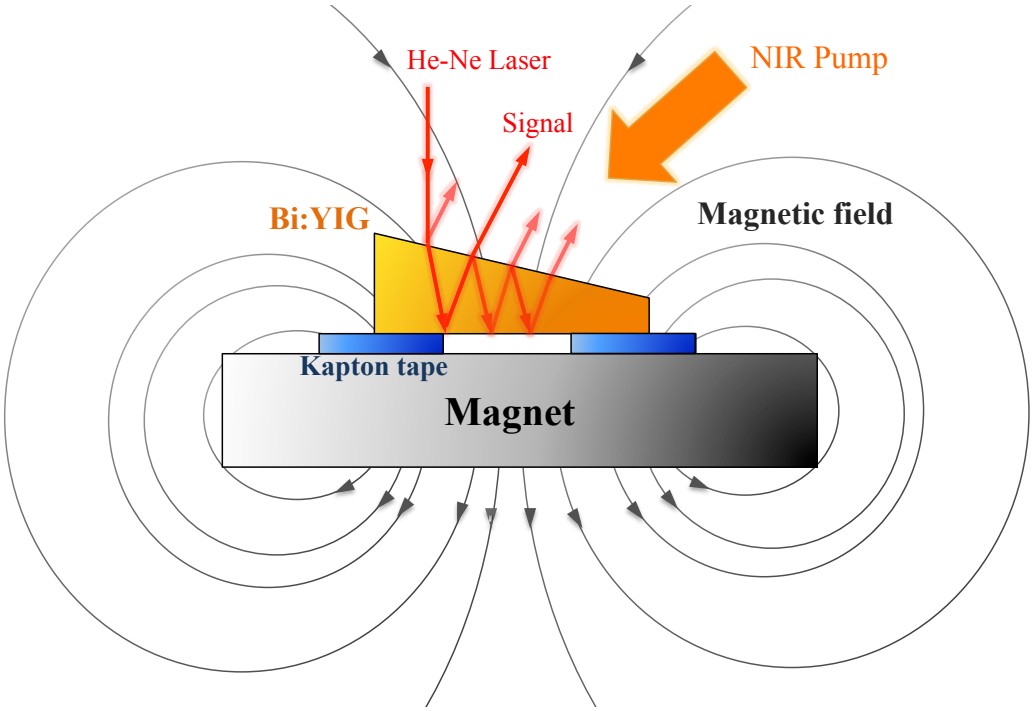

Figure 3.1: Scheme of the magnetic field detection with a wedged Bi:YIG crystal pumped with a NIR pump pulse and taped on a permanent magnet.

In figure 3.2 and 3.3 two different set of measurements are shown. The pump fluence was respectively 1.25 mJ/cm^2 and 3.05 mJ/cm^2.

The transverse magnetic field of the permanent magnet induces a magnetization in the Bi:YIG which microscopically corresponds to the spin of the electrons of the crystal aligned along the field lines. When the pump shines the sample two things happen simultaneously but on two separated time ranges: a Kerr effect is induced in the material, which is the reason behind the fast peak visible in 3.3. This phenomenon is fast and strongly dependent on the pump fluence. The longer time effect visible in both measurement sets is a long-lived decay on the equilibrium state due to a heating of the material: the pump transfers energy to the garnet heating it up and disordering the spins. With the slow cooling down process the equilibrium state is recovered.

In the 1.5 GHz measurement set some fast oscillations are visible. In figure 3.4 the Fourier transform of the signal is shown. The low frequency oscillation ($\sim$0.4 GHz) is noise due to the coupling with the Pockels cell of the Ti:Sapphire laser as explained in chapter 2.4. The fast oscillation is noise traceable to the GHz electronic of the ultrafast balance photodetector. Unfortunately those two noise contributions were really hard to get rid of but in the end we built a metal box to shield the EM field of the Pockels cell reducing a lot the first peak in the frequency domain.

The purpose of this experiment was to test the Bi:YIG as a detector in combination with the He-Ne laser and it worked as expected. The minimum detectable angle obtained with the configuration described is less than 1 μT, thus the noise level is around one order of magnitude larger than the shot noise limit.

I didn't investigate all the features of the Bi:YIG signal because it was not the purpose of the experiment. The material is characterized by strong magnons but in the 10 GHz regime, not detectable with the devices used.

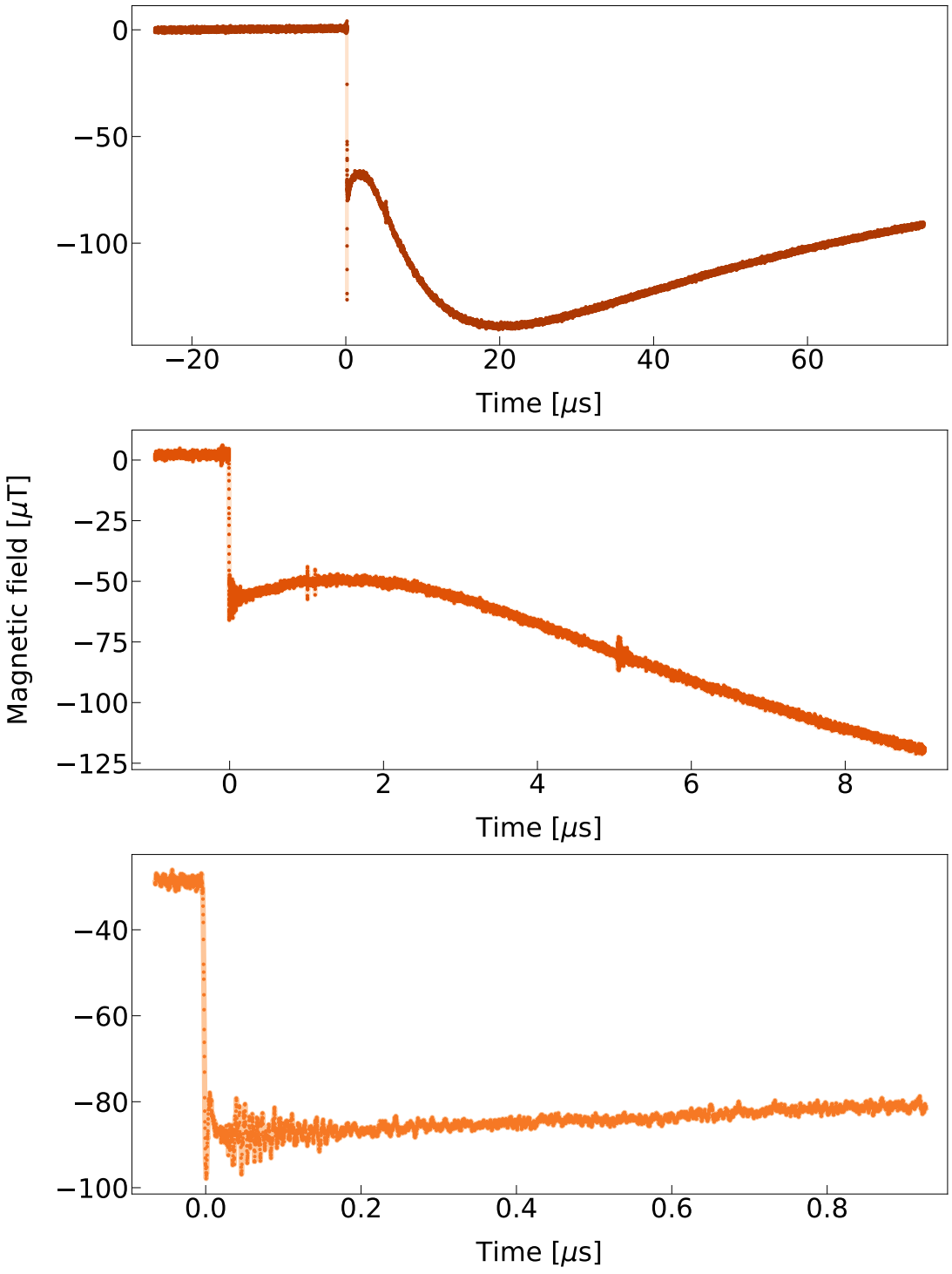

Figure 3.2: Three different time acquisition intervals of a NIR pump probe measurement on a wedged Bi:YIG slab, with pump fluence pf 1.25 mJ/cm^2 and detected with a 100 MHz balance photo-diode.

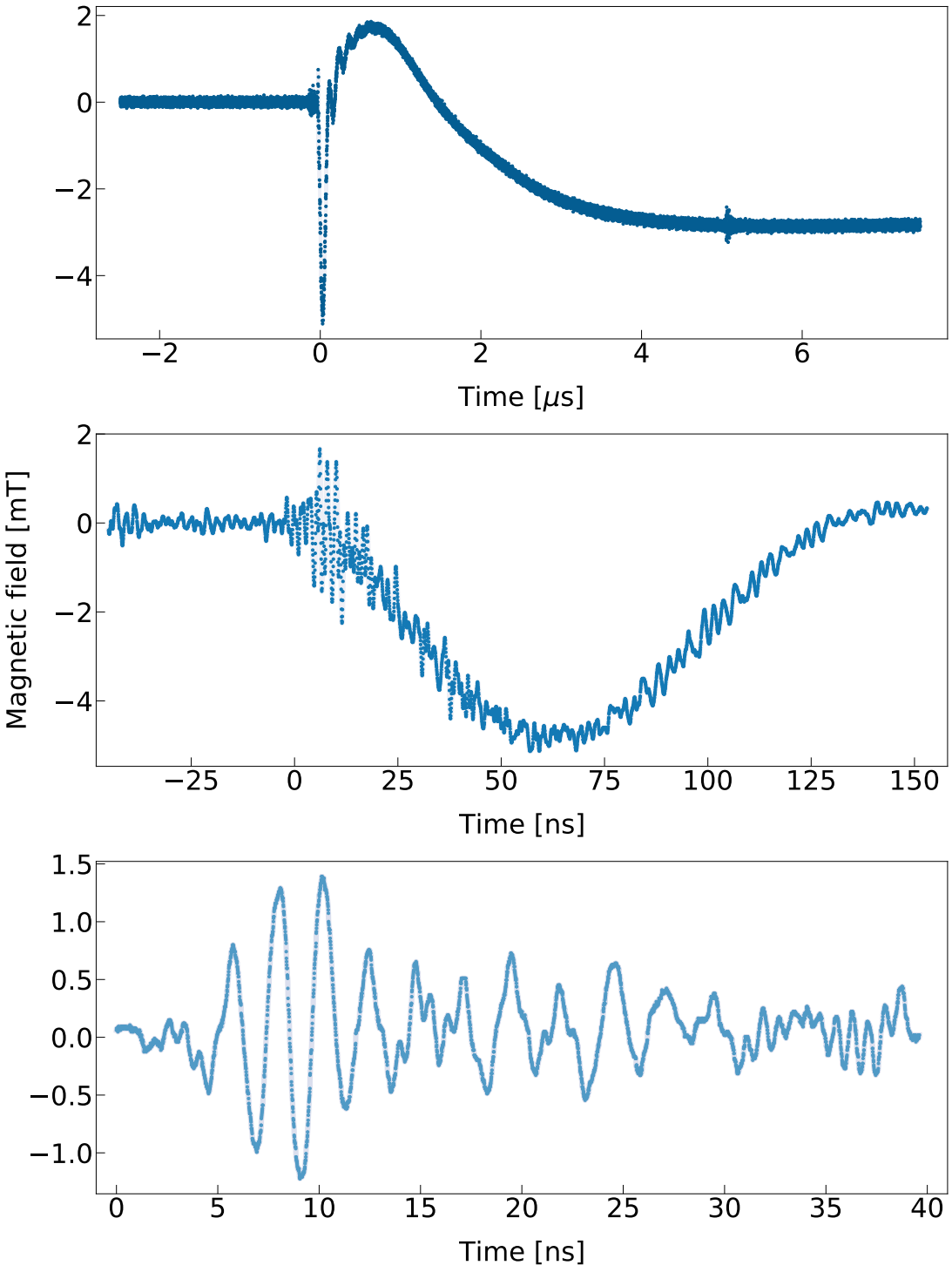

Figure 3.3: Three different time acquisition intervals of a NIR pump probe measurement on a wedged Bi:YIG slab, with pump fluence pf 3.05 mJ/cm^2 and detected with a 1.5 GHz balance photo-diode.

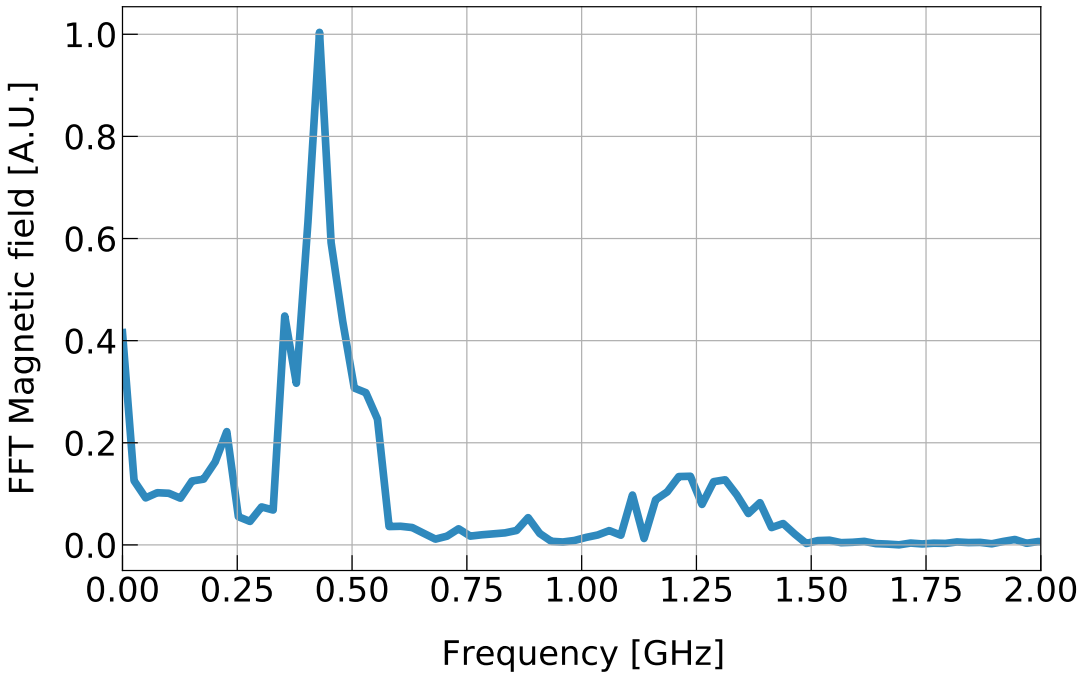

Figure 3.4: Spectrum of signal shown in figure 3.3.

Chapter 4

Towards probing the light-induced Meissner effect in K_3C_{60}

4.1 Previous evidence of a photo-induced superconductive state in K_3C_{60}

Fullerenes (e.g. C_{60} and C_{70}) are large, stable, spherical, hollow carbon based molecules, discovered in 1985 by Kroto et al. [32]. In 1991, the metallic behaviour of solid alkali-doped C_{60} has been shown by Haddon et al. [33]. Alkali-substituted compounds A_3C_{60} gained interest in the scientific community because of their superconductivity, characterized by relatively high transition temperature, bigger than any other organic superconductor, up to ∼33 K for $RbCs_2C_{60}$. The alkali atoms (K, Rb and Cs) dope the C_{60} structure altering the distance between the characteristic carbon buckyballs shaped carbon chains (figure 4.1, panel (a)). This change in the lattice spacing is crucial for the behaviour of these materials, as shown in figure 4.1.

K_3C_{60} was the focus of the research I carried on during my thesis project because of its high temperature superconductive features upon THz pumping. In the next paragraph I will summarize the main properties of this material.

The potassium doped fulleride K_3C_{60} has a metallic behaviour above T_c and a superconductive transition temperature of ∼19.8 K.

In 2015 Mitrano et al. presented evidences of an high temperature light-induced

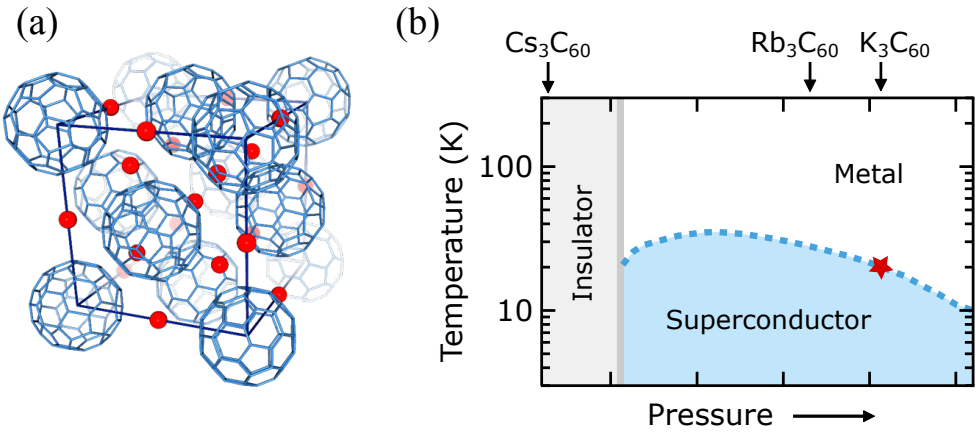

Figure 4.1: (a) Molecular structure of K_3C_{60}: cubic unit cell composed by C_{60} molecules (blue) with alkali atoms (red) placed in the interstitial spaces; (b) Phase diagram for alkali doped fullerenes (A=K,Rb,Cs). Increasing pressure is equivalent to decrease the lattice spacing (upper axis), which changes when the alkali atoms are changed. Lattice spacing of three characteristic compounds is marked with arrows on the upper axis. The red star indicates the superconductive critical temperature of K_3C_{60} at ambient pressure. Figure adapted from [34].

superconductive state in K_3C_{60}. In the experiment, K_3C_{60} powders are excited with femtosecond mid-infrared pulses with frequency from ∼20 THz to ∼50 THz: a spectral region in which the material has shown to be infrared active.
In figure 4.2, THz reflectivity R(ω) results are shown, together with real and imaginary part of optical conductivity $\sigma_1(\omega)$ and $\sigma_2(\omega)$[35]. It is evident the effect of the MIR pump on the K_3C_{60} powder, leading to an optical conductivity behaviour congruous with the equilibrium superconductive state measurement [3][36]. Mitrano et al. research was the first evidences of light-induced optical superconductivity in alkali-doped C_{60} compounds, further investigated under pressure by Cantaluppi et al. and its parametric amplification by Buzzi et al. in the next years. [37][38].

In 2021 Budden et al. achieved an astonishing result: generating mid-infrared pump pulses with tunable duration, ranging from one ps to one nanoseconds, they observed the same optical features characteristic of femtoseconds excitation timescale but on nanoseconds scale [4] [34]. Thus the superconductive state apparently becomes metastable after sufficiently strong optical driving, with lifetime longer than ten nanoseconds. This allowed Budden to measure directly the resistance

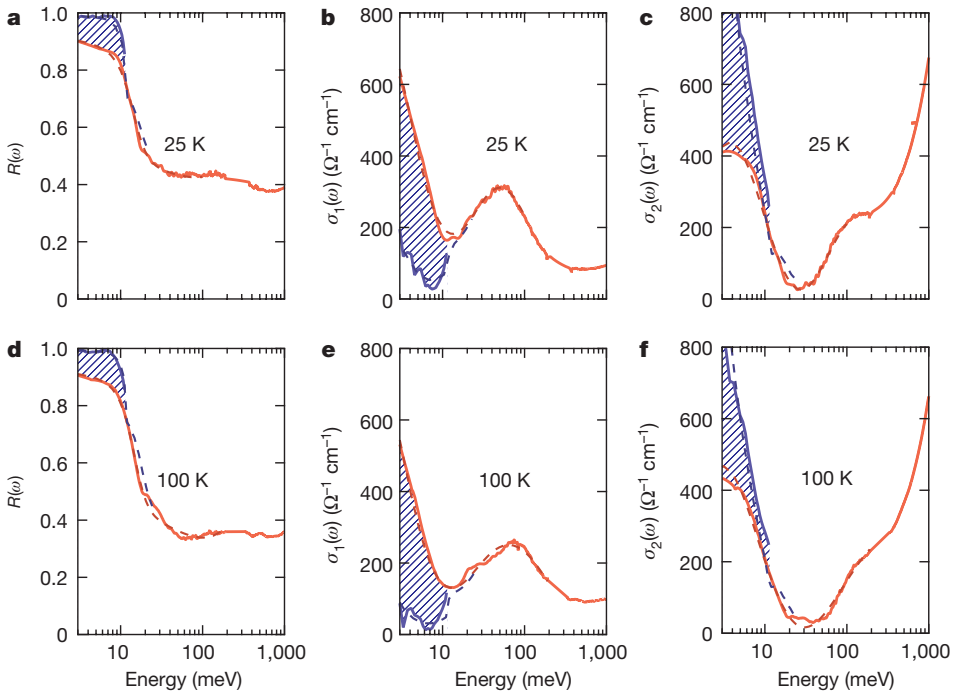

Figure 4.2: Transient optical response of photo-excited K_3C_{60} at T = 25 K (panel a–c) and T = 100 K (panel d–f). In red data taken at equilibrium and in blue data taken 1 ps after photo-excitation. Hatched regions highlight pump-induced changes. Pump fluence of 1.1 mJ/cm^2. Figure adapted from [3].

.

change of the process with a four-terminal sensing turning out into a vanishing resistance with same time features as the estimated by THz-conductivity (figure 4.3).

This reputably metastable light-induced superconductor gives access to physics regimes not reachable before. Having a superconductor generated with ultrafast techniques but with lifetime compatible with electronics opens up a wide range of possibility: first of all the study on the Meissner effect dynamics.
A fundamental characteristic of a superconductor, by definition, is the Meissner effect. A further, necessary proof to claim that K_3C_{60} becomes a superconductor upon MIR pumping is the Meissner effect itself. This grounds all this thesis project.

In the next chapter I will describe the setup, initially used by Budden et al. to measure the metastable K_3C_{60} state and adapted to the Meissner effect detection purpose on the same material. Furthermore I will provide a data set taken with

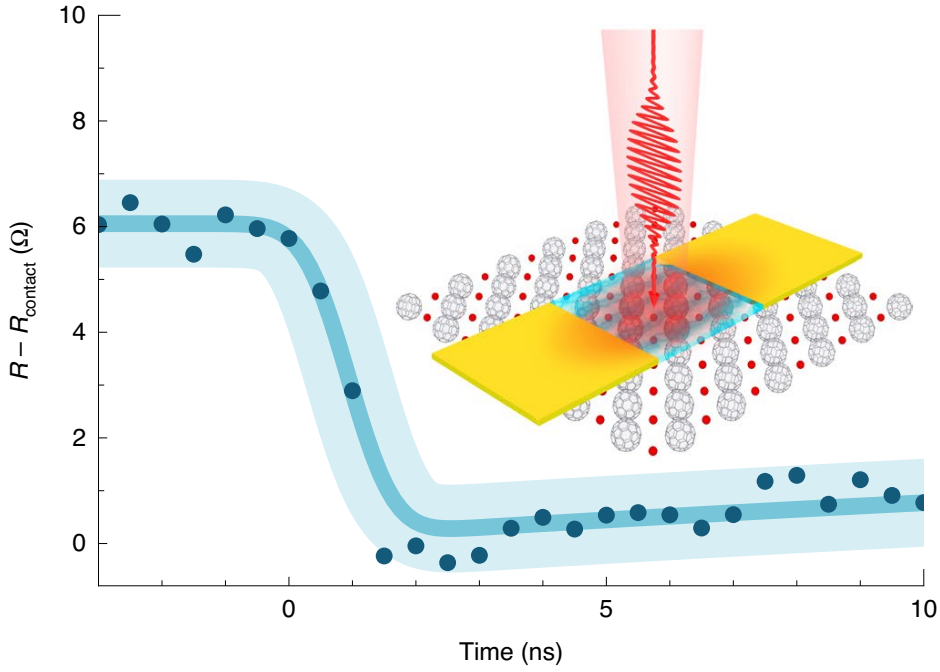

Figure 4.3: Resistance of a K_3C_{60} pellet embedded in a microstrip transmission line as function of time after photoexcitation, pumped with MIR pump, fluence $\sim$25 mJ/cm^2 and pump-pulse duration of 75 ps. The shaded region indicates the systematic error introduced by the resistance measurement calibration. The inset shows a schematic of the electrical transport experiment with gold electrodes on K_3C_{60} in yellow, the region of current flow in teal and the pump pulse in red. Figure adapted from [4].

.

a collective continuous-wave and ultrafast approach, probing superconductivity destruction, as a starting point to measure the superconductive light-induced state magnetic dynamics.

4.2 MIR pump setup with cryostat & variable magnetic field

4.2.1 MIR length tunable pump pulse generation

MIR pump pulse generation is not straightforward and makes use of a unique optical setup able to create high power THz pulses tunable in length, synchronized with a femtosecond laser [39].
The starting point is a commercial Ti:Al_2O_3 regenerative amplifier pumping an OPA. The signal and idler generated are use to get the THz seeding train of pulses, exploiting a difference frequency generation process in a 1.5 mm GaSe crystal. Part of these pulses is injected in a transversely excited atmosphere (TEA) CO_2 laser. The most intense pulse of the train out of the laser is selected with a Pockels cell and MIR wire grid polarizers. The pulse is then amplified in a ten-pass amplifier based on another commercial TEA CO_2 laser. The output pulse is 1.3 ns long, ∼11 mJ at 18 Hz repetition rate. Subsequently its duration is tuned using two silicon wafers: a pair of intense synchronized femtosecond pulses from the Ti:Al_2O_3 (800 nm wavelength, 100 fs duration) are used to photo-excite the semiconductor to create an electron-hole plasma at the surface. This plasma works like a mirror with ultrafast switching time and varying the time delay between the pair of pulses one can literally cut the THz pulse power obtaining a duration range between 5 ps and 1.3 ns. A scheme of the setup is shown in figure 4.4.

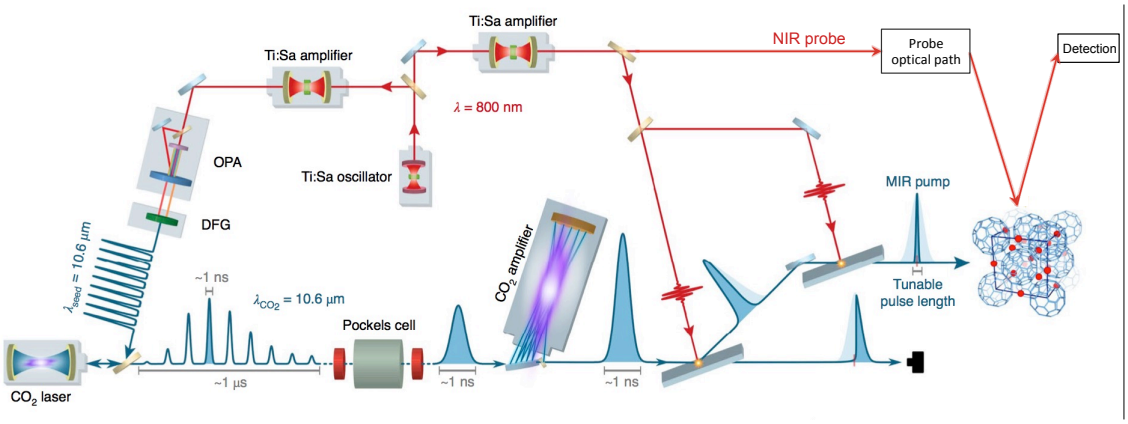

Figure 4.4: Experimental setup for THz high power, length tunable pulse generation. Adapted from [4].

.

4.2.2 MIR pump probe setup description

The magnetic field sensing technique is analogous as the one used on InSb and Bi:YIG described in chapters 2 and 3. A linearly polarized CW Helium-Neon laser beam (λ ∼633 nm) is used to measure the Faraday effect induced by pumping a K_3C_{60} pellet with a THz pump placed in a magnetic field.
The K_3C_{60} pellet is pressed onto the magneto-optic detector (Bi:YIG), separated by a thin aluminum layer. The sample is pumped on one side. The pump theoretically induces a change in the K_3C_{60} phase: if it becomes superconductive a shielding of the magnetic field is expected, at least of a certain percentage, changing the overall B field. The sticked detector induces a different polarization rotation in accordance with this magnetic field change. The probe beam shines only the Bi:YIG in order to avoid artifacts creation or sample heating. The aluminum foil is needed to increase the reflectivity of the magneto-optic detector and avoid penetration of the pump and of the probe in the other section.
The detection proceeds as a standard polarization rotation measurement with an half-wave plate, a Wollaston prism and a balance photodetector. The B field is generated with a coil controlled by a current generator. The setup, shown in figure 4.5, is placed in a high vacuum chamber and the sample is held at cryo temperature with a cryostat working with a liquid helium pumping system. The minimum working temperature used is 8 K for superconductivity destruction measurement.

All the CW probing is made in parallel with the ultrafast standard technique which makes use of a commercial Ti:Al_2O_3 probe laser ($\lambda \sim$ 800 nm, ∼100 fs pulse length). Engineering the double probing is straightforward: a long-pass filter (LPF) with ∼700 nm cut-off wavelength at is used as dichroic optics to mix and separate the two beams as can be seen in figure 4.6. Basically the LPF reflects with high efficiency the 633 nm beam but transmits the 800 nm beam. The same method is used to separate the beams after the sample in order to detect them separately.
The red Helium-Neon laser is fiber coupled in a polarization mantaining single-mode optical fiber and its beam diameter is controlled through an output fiber collimator. An input polarizer controls the input polarization of both the ultrafast and CW beams. The space resolution of the system is ∼35 μm and is referred to the probe beam diameter in the sample position.

4.2.3 Periodic magnetic field detection method

The purpose of the experiment is to measure a possible light-induced Meissner effect in K_3C_{60} pellet. An external magnetic field is applied to the sample. When the sample is metallic the magnetization follows the field lines. As soon as the material turns superconductive, the magnetic field is expelled and the overall B shape is changed. This variation is what we want to detect.

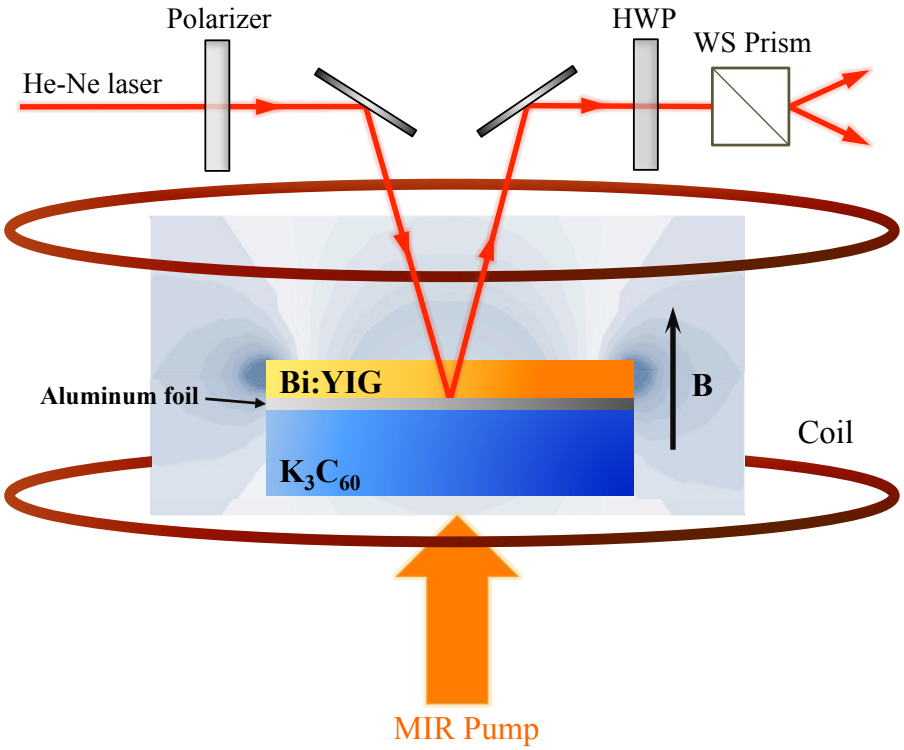

Figure 4.5: Meissner effect detection setup scheme. The sample pressed on a Bi:YIG slab used as a detector is placed in a magnetic field generated with a coil. The Faraday effect induced by the MIR pump on the K_3C_{60} sample is measured through a standard polarization rotation measurement.

In figure 4.7 the external magnetic field is shown. The field is alternated and generated starting from a square wave current function synchronized with the MIR pump pulse generation ∼10.6 Hz. Each field half-cycle is synchronized with a pump pulse arrival at ∼21.2 Hz. The field is oscillating between ±1.5 mT. The response of the field to a square wave current is of course not square but it has a certain rise time mainly due to Eddy currents.

In the ultrafast pump-probe method each point taken when the field is positive is subtracted from the corresponding negative field one. This procedure leads to an improvement of more than one order of magnitude in the SNR and it's important to cut off all the Flicker noise components of the measurement.

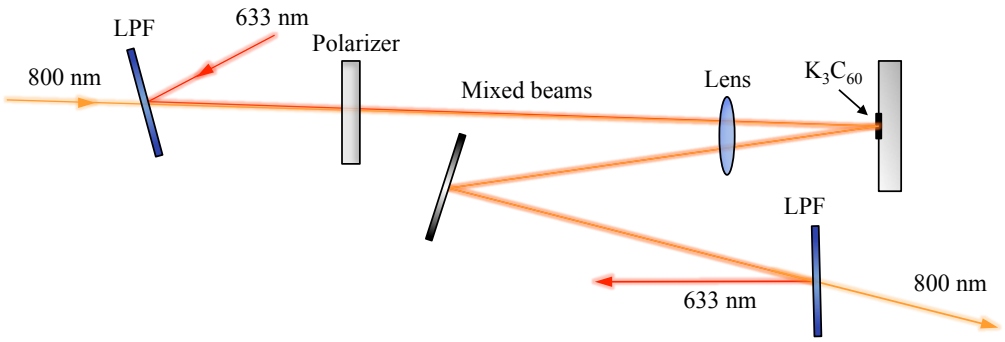

Figure 4.6: Optical configuration of the ultrafast and the CW probes. Two long-pass filter are used as dichroic optics to mix and separate the beams.

.

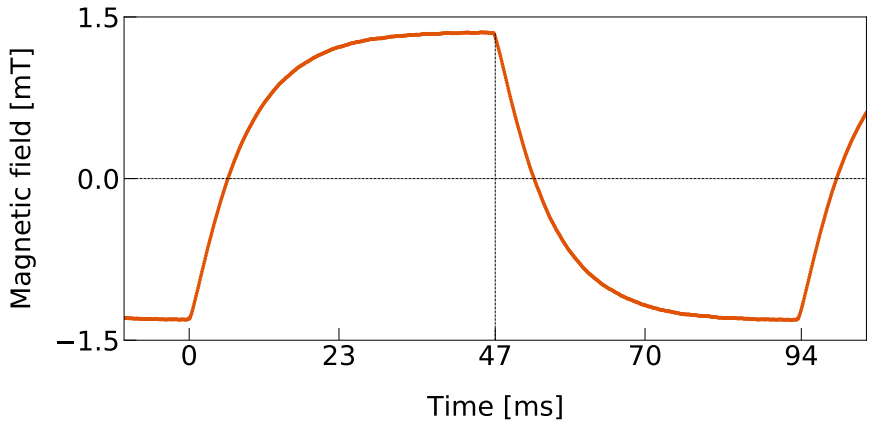

Figure 4.7: External magnetic field applied on the K_3C_{60} sample. The field has been measured with the CW probe setup.

In the continuous-wave configuration subtracting two subsequential waveforms ($B^{(+)}$ and $B^{(-)}$ is not trivial and we developed an scheme exploiting an electronic switch (figure 4.8)

The CO_2 discharge triggers the balance detection, such that it is synchronized with the pump pulse arrival, and the current generation, made with an electronic current generator. The current flows in a coil surrounding the sample and generating the magnetic field. The output signal of the balanced detection is sent through an

electronic switcher[1]. The switcher is controlled by the magnetic field itself: when it is positive the output is sent on one channel and the other one is kept to zero, and viceversa. Thus the oscilloscope records two channels: one corresponding to $B^{(+)}$ and one corresponding to $B^{(-)}$. The data are transferred on the PC and stored. Afterwards a subtraction of the two dataset $B^{(+)}$ and $B^{(-)}$) is performed in order to get rid of the law frequency noise.

[1]ZASWA-2-50DRA+ Absorptive SPDT, Solid State Switch, DC - 5000 MHz, 50Ω; by Mini-Circuits.

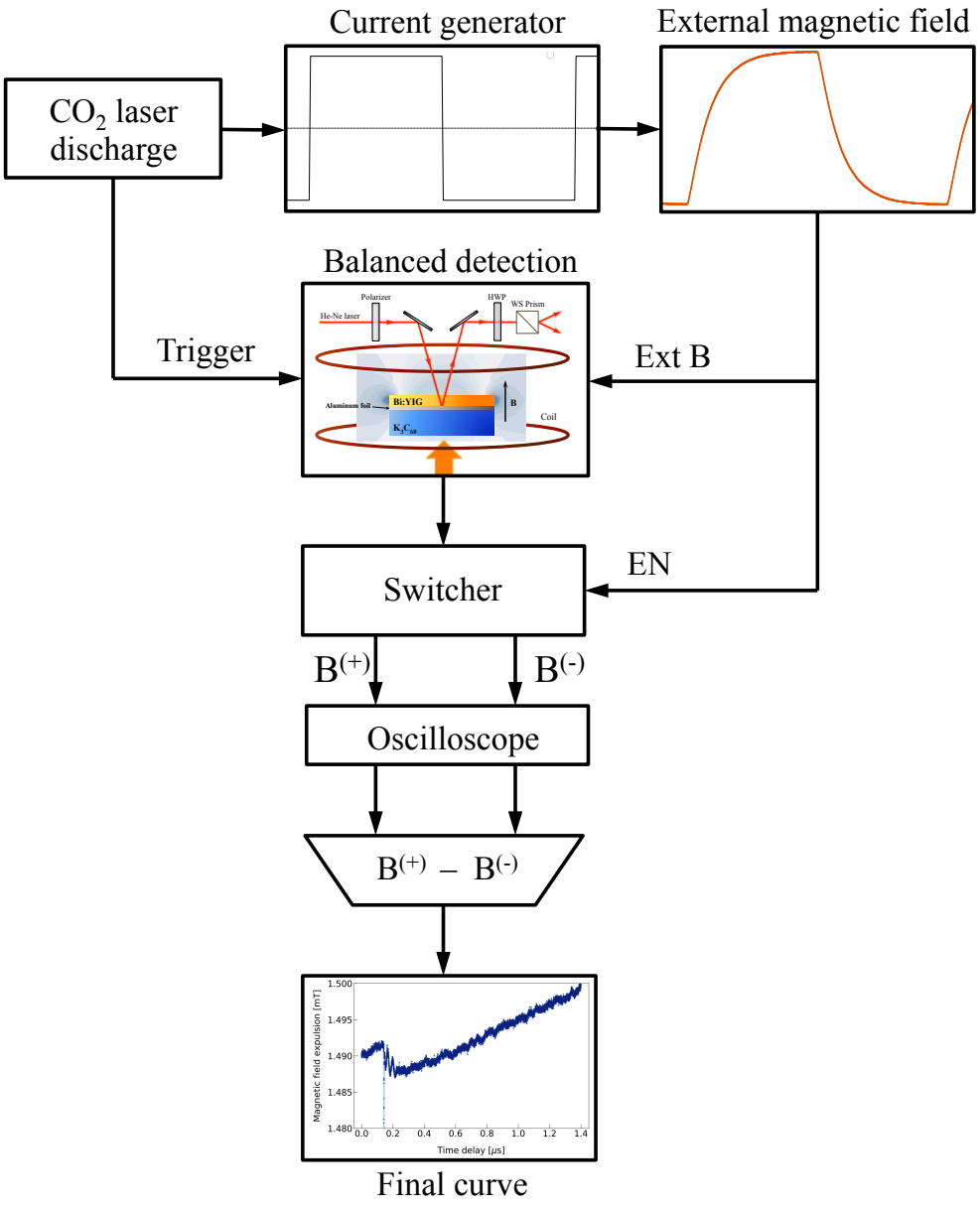

Figure 4.8: Acquisition with a CW laser complete scheme. The CO_2 laser discharge triggers the balanced detection and the alternated magnetic field which controls an electronic switch. The latter is used to acquire separately the signal curves when the magnetic field is positive ($B^{(+)}$) and negative $B^{(-)}$). A final digital subtraction of the two acquisition is performed. This procedure is done in order to reduce the low frequency noise contribution and increase the SNR.

.

4.3 Time-resolved measurement of superconductivity destruction by a MIR pulse

To ultimately characterize the proposed setup we decide to measure a mid-infrared pump superconductivity destruction in the fullerede K_3C_{60}.
When the superconductor (SC) below T_c is pumped we expect a perturbation in the superconductive order which leads to a destruction of the superconductivity for a certain time interval. This mechanism can be related to some disorder introduced by the pump, probably due to heating of the sample.

In figure 4.9 a model of a SC magnetization in a varying external magnetic field is proposed.
A square wave B is applied to a SC. When the SC is kept above T_c its behaviour is metallic and the magnetization follows perfectly the external field **(a)**. If the SC is below T_c and it has an ideal behaviour it shields completely the external field because of the Meissner effect **(b)**. If the SC is not ideal there is a certain field penetration in the material which leads to a partial shield **(c)**. Upon MIR pumping the superconductivity is destroyed and recovered, with consequently penetration and re-shielding of the field **(d)**

Let us look at figure 4.10. The external field is a square wave oscillating between ± 1 a.u. We consider a general field cycle. In the case shown the Meissner effect leads to a partial shielding of the external field (α), thus the magnetization follows the external field up to $\pm(1-\alpha)$ (Step **(A)** in figure). When the pump shines the SC it destroys the superconductivity: the external B field penetrates the material whose magnetization becomes ± 1 (Step **(B)** in figure). After a certain time the superconductivity is restored because the system is continuously cooled by a liquid helium flow. The restored magnetization function is called "field cooled" since the the not-ideal SC shields the external field but part of it remains trapped in the SC (F_{res}) (Step **(C)** in figure). Then the cycle is repeated. An attempt to calculate the magnetization of the SC in the three different step of the process is given with reference to a general external magnetic field with 1 a.u. amplitude:

$$M^{(A)} = (1-\alpha) - \alpha(1-F_{res}) = 1 - 2\alpha + \alpha F_{res} \tag{4.1}$$

$$M^{(B)} = (1-\alpha) + \alpha = 1 \tag{4.2}$$

$$M^{(C)} = (1-\alpha) + \alpha(1-F_{res}) = 1 - \alpha F_{res} \tag{4.3}$$

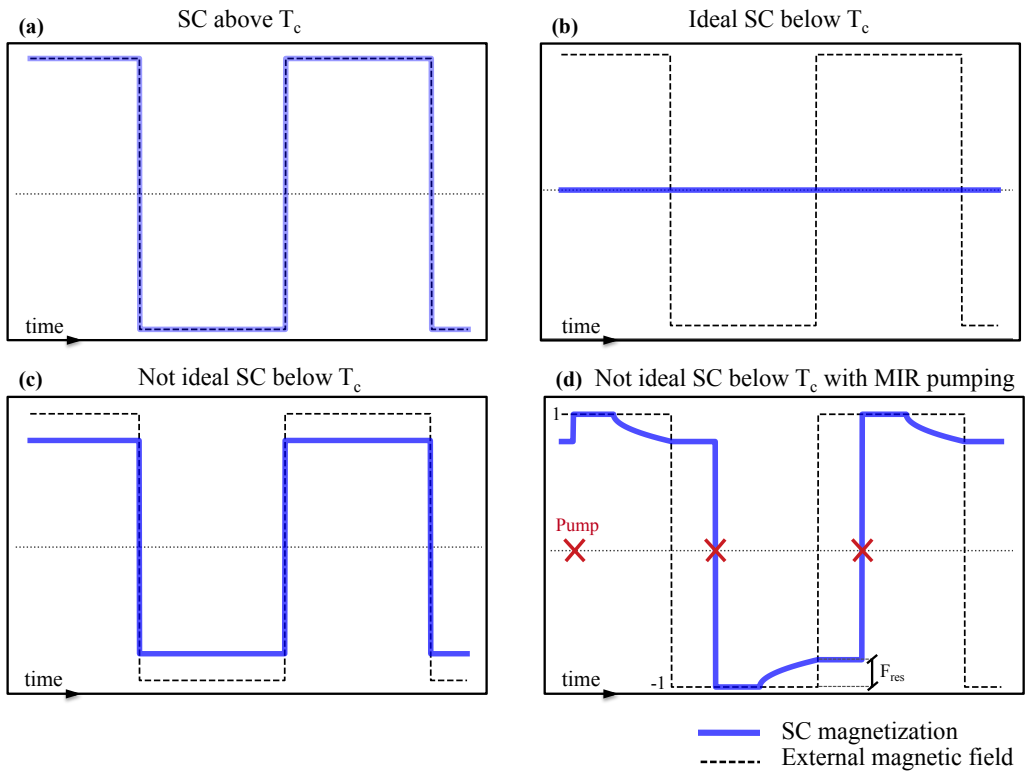

Figure 4.9: Model of a superconductor (SC) magnetization (blue line) in a varying external magnetic field (dotted line). **(a)** SC above T_c which is a classic metallic course; **(b)** Ideal SC below T_c which shields completely the external field; **(c)** Not ideal SC below T_c which shields only a fraction of the external field. The remaining field penetrates the SC. **(d)** Not ideal SC below T_c pumped with MIR pulses which destroy the superconductivity. The SC becomes metallic for a certain time until the superconductivity is recovered but with a partial field shielding.

If we suppose to have a SC with $\alpha = 0.1$ and $F_{res} = 0.2$ we expect a magnetization respectively of:

$$M^{(A)} = 0.82 \ a.u.$$
$$M^{(B)} = 1 \ a.u.$$
$$M^{(C)} = 0.98 \ a.u.$$

The model explained is a starting point to understand and predict the experimental

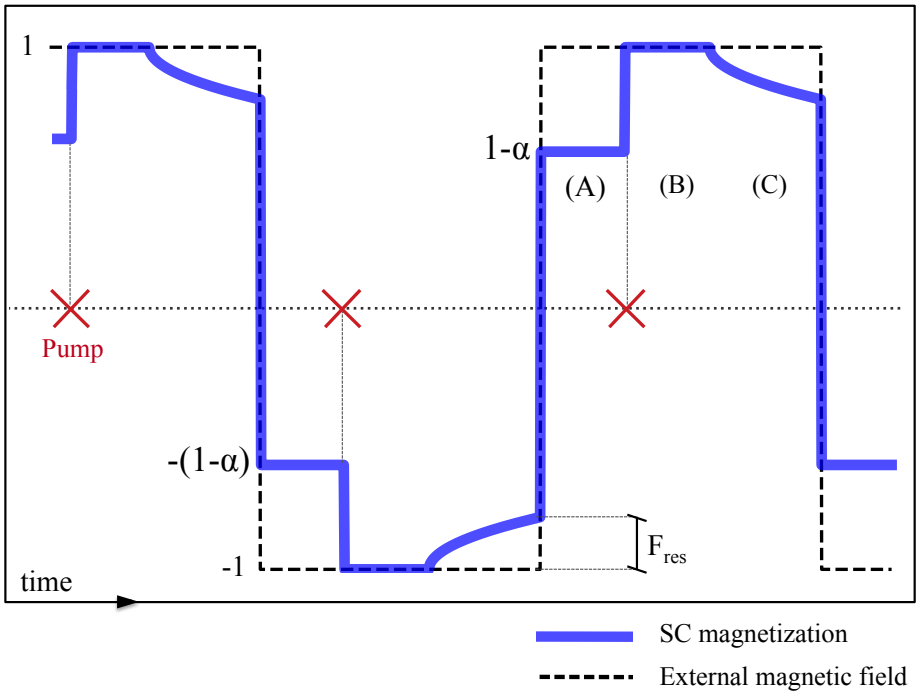

Figure 4.10: Model of the superconductivity destruction by an intense light pulse (red crosses). The superconductor represented is not ideal, therefore it doesn't shield completely the external magnetic field applied. When the pump shines the sample, the superconductivity is destroyed and partially recovered, with a further penetration of field in the superconductor.

results obtained destroying the superconductivity in K_3C_{60} with a MIR intense pulse.

In figure 4.11 a time-resolved superconductivity destruction measurement on a K_3C_{60} pellet is shown. The sample is held at T = 8 K. Two pump fluences have been used. CW space resolution = ∼35 μm. Time resolution = 3.2 ns.
The result is fitting qualitatively with the simplified model explained before and with an evident destruction and recover of the superconductive phase. With an external magnetic field of ∼1.5 mT, a 2% field expulsion is reached. The peak at time zero and the visible 200 kHz oscillations are due to a coupling of the CO_2 laser discharge with the balanced photodetector. Data on shorter time windows can be taken with the ultrafast setup whose performances would be more reliable.

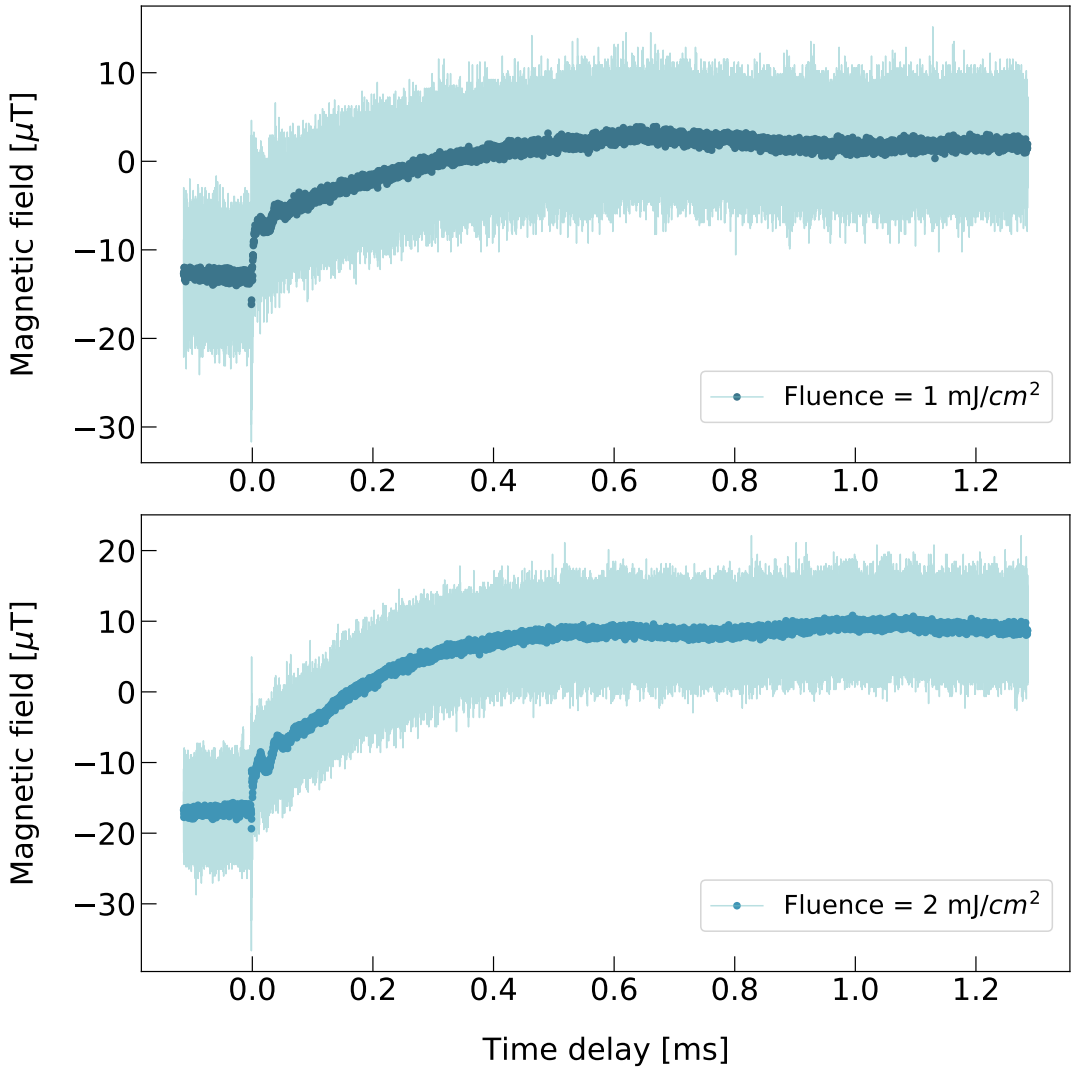

Figure 4.11: Superconductivity destruction time resolved measurement upon mid-infrared pump on a K_3C_{60} pellet. T = 8 K. Fluence = 1 mJ/cm^2 and 2 mJ/cm^2. Time resolution of the measurement: 3.2 ns, The dark curves are the binned data with a bin-step of 200 ns. The light-blue functions are the raw data to evidence the variance of the datasets.

Conclusion & Outlook

In this thesis work I entirely developed a new magnetic field detection technique based on a continuous-wave laser pump probe configuration. The project aims to work in parallel with an ultrafast pump probe setup to sense a possible light-induced Meissner effect in alkali-doped fullerides. Started from the theoretical background, I described all the research and development phases, the instrument selection and performances and the test results obtained on an indium antimonide slab, a wedged bismuth-substituted yittrium-iron garnet slab and on the interesting and exciting K_3C_{60}. The first attempts aimed at sensing a light-induced superconductivity destruction on K_3C_{60} and the result is satisfying and fits qualitatively with our theoretical model. The definitive features of the new CW pump probe are a minimum reached sensitivity of 0.6 μRad/$\sqrt{\text{Hz}}$; a space resolution of $\sim$35 μm and an astonishing minimum time resolution of 500 ps. The latter is the real innovation of this technique, which combines ultrafast electronics with stable and reliable optics. The whole probe configuration is relatively cheap since it's based on a commercial helium-neon laser. The acquisition time reached is much lower than the time needed for the same time-window acquisition with the parallel ultrafast technique i.e. 40 minutes instead of 6 hours. These are the reasons why it will be employed for the first analysis and characterization of the samples. To be more specific, if one wants to probe the Meissner effect on a alkali-doped fulleride, he must check in advance if the sample is not oxidized and if it shows superconductivity. To do so a quick scan with the CW setup suits perfectly, saving time, costs and energy.

So far no signal has been seen in the light-induced Meissner effect experiment. Probably a further improvement on the sensitivity should be implemented. New sample configuration are going to be tested.

Looking at the future, this method can be used in many other magnetic field sensing experiments which need a fast sub-nanosecond detection with space and cost saving. Light-driven magnets with metastable states have already been observed and, unlike with magneto-optic Kerr effect, this Faraday effect based technique allows to observe antiferromagnet states because of the bulk feature of the polarization rotation effect.

The possible improvement directions are the reduction of the noise due to the coupling of external electronics with the balanced photodetectors; the increase of the SNR with the employment of a more powerful laser and an advancment of the method with the use of a ultrafast camera to resolve in space the sample information and create a quasi-real time map of the magnetic field with a non-invasive, low power and flexible technique.

Bibliography

[1] Elliot Snider, Nathan Dasenbrock-Gammon, Raymond McBride, Mathew Debessai, Hiranya Vindana, Kevin Vencatasamy, Keith V. Lawler, Ashkan Salamat, and Ranga P. Dias. «Room-temperature superconductivity in a carbonaceous sulfur hydride». In: *Nature* 586.7829 (Oct. 2020), pp. 373–377. ISSN: 1476-4687. DOI: 10.1038/s41586-020-2801-z. URL: https://doi.org/10.1038/s41586-020-2801-z (cit. on p. 1).

[2] R. Mankowsky et al. «Optically induced lattice deformations, electronic structure changes, and enhanced superconductivity in YBa2Cu3O6.48». In: *Structural Dynamics* 4.4 (2017), p. 044007. DOI: 10.1063/1.4977672. URL: https://doi.org/10.1063/1.4977672 (cit. on p. 1).

[3] M et al. Mitrano. «Possible light-induced superconductivity in K3C60 at high temperature». In: *Nature* 530 (2016), pp. 461–4. URL: doi:10.1038/nature16522 (cit. on pp. 1, 38, 39).

[4] M. Budden et al. «Evidence for metastable photo-induced superconductivity in K3C60». In: *Nature Physics* 17.5 (May 2021), pp. 611–618. ISSN: 1745-2481. DOI: 10.1038/s41567-020-01148-1. URL: https://doi.org/10.1038/s41567-020-01148-1 (cit. on pp. 1, 38, 40, 41).

[5] Iris Crassee, Julien Levallois, Andrew L. Walter, Markus Ostler, Aaron Bostwick, Eli Rotenberg, Thomas Seyller, Dirk van der Marel, and Alexey B. Kuzmenko. «Giant Faraday rotation in single- and multilayer graphene». In: *Nature Physics* 7.1 (Jan. 2011), pp. 48–51. ISSN: 1745-2481. DOI: 10.1038/nphys1816. URL: https://doi.org/10.1038/nphys1816 (cit. on p. 3).

[6] M. Mansuripur. «The Faraday Effect». In: *Opt. Photon. News* 10.11 (Nov. 1999), pp. 32–36. DOI: 10.1364/OPN.10.11.000032. URL: http://www.osa-opn.org/abstract.cfm?URI=opn-10-11-32 (cit. on p. 3).

[7] D. Vojna, O. Slezák, A. Lucianetti, and Mocek. «Verdet Constant of Magneto-Active Materials Developed for High-Power Faraday Devices». In: *Appl. Sci.* 9 (15 Aug. 2019), p. 3160. URL: https://doi.org/10.3390/app9153160 (cit. on p. 3).

[8] R. Fenici, D. Brisinda, and A. M. Meloni. «Clinical application of magnetocardiography». In: *Expert Rev Mol Diagn* 5.3 (May 2005), pp. 291–313 (cit. on p. 4).

[9] Matti Hämäläinen, Riitta Hari, Risto J. Ilmoniemi, Jukka Knuutila, and Olli V. Lounasmaa. «Magnetoencephalography—theory, instrumentation, and applications to noninvasive studies of the working human brain». In: *Rev. Mod. Phys.* 65 (2 Apr. 1993), pp. 413–497. DOI: 10.1103/RevModPhys.65.413. URL: https://link.aps.org/doi/10.1103/RevModPhys.65.413 (cit. on p. 4).

[10] Yiming Deng, Yuhua Cheng, Liang Xuan, and Zhiwei Zeng. «Principles of Magneto-optic Imaging and Its Applications». In: *Integrated Imaging and Vision Techniques for Industrial Inspection: Advances and Applications*. Ed. by Zheng Liu, Hiroyuki Ukida, Pradeep Ramuhalli, and Kurt Niel. London: Springer London, 2015, pp. 483–536. ISBN: 978-1-4471-6741-9. DOI: 10.1007/978-1-4471-6741-9_15. URL: https://doi.org/10.1007/978-1-4471-6741-9_15 (cit. on p. 4).

[11] Michael R. Koblischka and Anjela Koblischka-Veneva. «MO-Imaging of Granular And Structured High-Tc Superconductors». In: (2004). Ed. by Tom H. Johansen and Daniel V. Shantsev, 71–78" (cit. on p. 4).

[12] T. H. Johansen, P. E. Goa, D. V. Shantsev, E. I. Il'yashenko, Y. M. Galperin, Å. A. F. Olsen, and M. Baziljevich. «Magneto-Optical Imaging of Superconducting Vortices». In: (2004). Ed. by Tom H. Johansen and Daniel V. Shantsev, pp. 53–60 (cit. on p. 4).

[13] Chun-Yeol You and Sung-Chul Shin. «Derivation of simplified analytic formulae for magneto-optical Kerr effects». In: *Applied Physics Letters* 69.9 (1996), pp. 1315–1317. DOI: 10.1063/1.117579. URL: https://doi.org/10.1063/1.117579 (cit. on p. 5).

[14] Ajit Srivastava, Meinrad Sidler, Adrien V. Allain, Dominik S. Lembke, Andras Kis, and A. Imamoğlu. «Valley Zeeman effect in elementary optical excitations of monolayer WSe2». In: *Nature Physics* 11.2 (Feb. 2015), pp. 141–147. ISSN: 1745-2481. DOI: 10.1038/nphys3203. URL: https://doi.org/10.1038/nphys3203 (cit. on p. 5).

[15] Wanxiang Feng, Jan-Philipp Hanke, Xiaodong Zhou, Guang-Yu Guo, Stefan Blügel, Yuriy Mokrousov, and Yugui Yao. «Topological magneto-optical effects and their quantization in noncoplanar antiferromagnets». In: *Nature Communications* 11.1 (Jan. 2020), p. 118. ISSN: 2041-1723. DOI: 10.1038/s41467-019-13968-8. URL: https://doi.org/10.1038/s41467-019-13968-8 (cit. on p. 5).

[16] T. Janda, L. Nádvorník, J. Kuchařík, D. Butkovičová, E. Schmoranzerová, F. Trojánek, and P. Němec. «Voigt effect-based wide-field magneto-optical microscope integrated in a pump-probe experimental setup». In: *Review of Scientific Instruments* 89.7 (2018), p. 073703. DOI: 10.1063/1.5023183. URL: https://doi.org/10.1063/1.5023183 (cit. on p. 5).

[17] Tianshu Lan, B. Ding, and Bilu Liu. «Magneto-optic effect of two-dimensional materials and related applications». In: Wiley-VCH GmbH, 2020 (cit. on p. 5).

[18] Dmitry Budker and Michael Romalis. «Optical magnetometry». In: *Nature Physics* 3.4 (Apr. 2007), pp. 227–234. ISSN: 1745-2481. DOI: 10.1038/nphys566. URL: https://doi.org/10.1038/nphys566 (cit. on p. 5).

[19] Florian Wolfgramm, Alessandro Cerè, Federica A. Beduini, Ana Predojević, Marco Koschorreck, and Morgan W. Mitchell. «Squeezed-Light Optical Magnetometry». In: *Physical Review Letters* 105.5 (July 2010). ISSN: 1079-7114. DOI: 10.1103/physrevlett.105.053601. URL: http://dx.doi.org/10.1103/PhysRevLett.105.053601 (cit. on p. 5).

[20] I. K. Kominis, T. W. Kornack, J. C. Allred, and M. V. Romalis. «A subfemtotesla multichannel atomic magnetometer». In: *Nature* 422.6932 (Apr. 2003), pp. 596–599. ISSN: 1476-4687. DOI: 10.1038/nature01484. URL: https://doi.org/10.1038/nature01484 (cit. on p. 5).

[21] Andrei Kirilyuk, Alexey V. Kimel, and Theo Rasing. «Ultrafast optical manipulation of magnetic order». In: *Rev. Mod. Phys.* 82 (3 Sept. 2010), pp. 2731–2784. DOI: 10.1103/RevModPhys.82.2731. URL: https://link.aps.org/doi/10.1103/RevModPhys.82.2731 (cit. on p. 6).

[22] J. Peatross and M. Ware. *Physics of Light and Optics*. 2015. Chap. 6. URL: optics.byu.edu (cit. on pp. 7, 12).

[23] G. Brooker. *Modern Classical Optics*. Oxford University Press, 2002 (cit. on p. 10).

[24] J. Peatross and M. Ware. *Physics of Light and Optics*. 2001. Chap. 3 and 4. URL: optics.byu.edu (cit. on p. 12).

[25] J.F. Cox. *Fundamentals of Linear Electronics: Integrated and Discrete*. Delmar Thomson Learning, 2002. ISBN: 9780766830189. URL: https://books.google.co.uk/books?id=FbezraN9tvEC (cit. on p. 17).

[26] M. Nisoli. *Semiconductor Photonics*. Società Editrice Esculapio, 2016 (cit. on p. 26).

[27] C.C. Gerry and P.L. Knight. *Introductory Quantum Optics*. Cambridge University Press, 2005. Chap. 7 (cit. on p. 26).

[28] T. Aichele, A. Lorenz, R. Hergt, and P. Görnert. «Garnet layers prepared by liquid phase epitaxy for microwave and magneto-optical applications – a review». In: *Crystal Research and Technology* 38 (7-8 July 2003), pp. 575–587. URL: https://doi.org/10.1002/crat.200310071 (cit. on p. 31).

[29] Weizhong Zhao. «Magneto-optic properties and sensing performance of garnet YbBi:YIG». In: *Sensors and Actuators A: Physical* 89.3 (2001), pp. 250–254. ISSN: 0924-4247. DOI: https://doi.org/10.1016/S0924-4247(00)00560-4. URL: https://www.sciencedirect.com/science/article/pii/S0924424700005604 (cit. on p. 31).

[30] Marwan Deb, Elena Popova, Michel Hehn, Niels Keller, Sébastien Petit-Watelot, Matias Bargheer, Stéphane Mangin, and Gregory Malinowski. «Damping of Standing Spin Waves in Bismuth-Substituted Yttrium Iron Garnet as Seen via the Time-Resolved Magneto-Optical Kerr Effect». In: *Phys. Rev. Applied* 12 (4 Oct. 2019), p. 044006. DOI: 10.1103/PhysRevApplied.12.044006. URL: https://link.aps.org/doi/10.1103/PhysRevApplied.12.044006 (cit. on p. 31).

[31] P. X. Zhang, D. J. Lockwood, and H. J. Labbe´. «Magnon and acoustic-phonon light scattering from Bi-doped yttrium iron garnet». In: *Phys. Rev. B* 48 (9 Sept. 1993), pp. 6099–6103. DOI: 10.1103/PhysRevB.48.6099. URL: https://link.aps.org/doi/10.1103/PhysRevB.48.6099 (cit. on p. 31).

[32] H. Kroto, J. Heath, and S. et al. O'Brien. «C60: Buckminsterfullerene». In: *Nature* 318 (1985), pp. 162–163. URL: https://doi.org/10.1038/318162a0 (cit. on p. 37).

[33] R. C. Haddon et al. «Conducting films of C60 and C70 by alkali-metal doping». In: *Nature* 350.6316 (Mar. 1991), pp. 320–322. ISSN: 1476-4687. DOI: 10.1038/350320a0. URL: https://doi.org/10.1038/350320a0 (cit. on p. 37).

[34] M. J. Budden. «Metastable Light-Induced Superconductivity in K3C60». PhD thesis. 2020 (cit. on p. 38).

[35] L. Degiorgi, G. Briceno, M. S. Fuhrer, A. Zettl, and P. Wachter. «Optical measurements of the superconducting gap in single-crystal K3C60 and Rb3C60». In: *Nature* 369.6481 (1994), pp. 541–543. DOI: 10.1038/369541a0 (cit. on p. 38).

[36] A. Cantaluppi. «Tuning light-induced superconductivity in K3C60». PhD thesis. 2017 (cit. on p. 38).

[37] A. Cantaluppi et al. «Pressure tuning of light-induced superconductivity in K3C60». In: *Nature Physics* 14.8 (May 2018), pp. 837–841. ISSN: 1745-2481. DOI: 10.1038/s41567-018-0134-8. URL: http://dx.doi.org/10.1038/s41567-018-0134-8 (cit. on p. 38).

[38] Michele Buzzi et al. «Higgs-Mediated Optical Amplification in a Nonequilibrium Superconductor». In: *Physical Review X* 11.1 (2021). DOI: 10.1103/physrevx.11.011055 (cit. on p. 38).

[39] M. Budden, T. Gebert, and A. Cavalleri. «Hybrid CO2-Ti:sapphire laser with tunable pulse duration for mid-infrared-pump terahertz-probe spectroscopy». In: *Opt. Express* 29.3 (Feb. 2021), pp. 3575–3583. DOI: 10.1364/OE.415140. URL: http://www.opticsexpress.org/abstract.cfm?URI=oe-29-3-3575 (cit. on p. 41).